Cement and Concrete Composites 143 (2023) 105262

Contents lists available at ScienceDirect

Cement and Concrete Composites

journal homepage: www.elsevier.com/locate/cemconcomp

Assessment of lithium slag as a supplementary cementitious material: Pozzolanic activity and microstructure development

SM Arifur Rahman [a], Aaron Dodd [b], Sanjida Khair [a], Faiz Uddin Ahamed Shaikh [a,*], Prabir Kumar Sarker [a], Anwar Hosan [a]

[a] Civil Engineering Discipline, School of Civil and Mechanical Engineering, Curtin University, Perth, Australia
[b] John de Laeter Research Centre, Department of Physics, Curtin University, Perth, Australia

ARTICLE INFO

Keywords:
Lithium slag
Pozzolanic activity
Frattini test
R^3 test
Microstructure

ABSTRACT

In this study, lithium slag was utilised as a supplementary cementitious material (SCM) to develop pozzolanic activity and reduce CO_2 emissions related to cement production, with a focus on comprehensive chemical tests and microstructural assessments. Lithium slag was primarily characterised through laser particle size analyser, X-ray fluorescence, X-ray diffraction, scanning transmission electron microscopy coupled with energy dispersive X-ray spectroscopy, and thermogravimetry. These tests indicate that lithium slag holds 31.6% amorphous phase with rich aluminosilicate minerals, making it an excellent candidate as pozzolan. The unsaturated lime and electrical conductivity pozzolanic activity precursor tests evaluated the potentiality of using lithium slag as a low carbon pozzolan. The optimum percentage of lithium slag as a supplementary cementitious material was determined from Frattini, strength activity index, and R^3 tests by replacing 0–60% cement. Results show that 40% lithium slag mortar could achieve 93% strength activity index in 28 days. The microstructure development of lithium slag was assessed and ettringite, monocarboaluminate, and intermixed calcium aluminosilicate hydrates were formed at 56 days.

1. Introduction

Supplementary cementitious materials (SCM) have been known for over fifty years. It is used as a partial replacement of cement, and an optimized proportion helps to develop the mechanical, durability, and microstructural properties of concrete. Using SCM will reduce cement demand for concrete construction and, thereby, reduce carbon footprint [1]. Lithium slag is generated from lithium refinery plants and predominantly composed of silicon, aluminium, calcium, and iron, with small amounts of light metals, making it an excellent candidate for use as SCM [1–6]. Previous studies explored various recycling methods of lithium slag, especially as a construction material, which encompass its incorporation in concrete production by partially replacing cement [2–4,7–14], its use in alkali-activated binder [15–19], as backfill [20,21], fine aggregate [22], light weight aggregate [23], and in manufacturing of bricks [24]. Researchers are also using lithium slag as a SCM without calcination or mechanical activation, as its silica-alumina rich oxide composition, amorphous content, and mineral phases in amorphous state provides a remarkable advantage to enhance the pozzolanic activity [2,25]. The aim of this research is to utilize lithium slag as a SCM to reduce CO_2 emissions related to cement production.

Lithium is extracted from the minerals spodumene, lepidolite, petalite, or zinnwaldite [26]. Primarily, the lithium rich minerals are mixed with sulfate salts and lime, chlorine, or carbonate salts, followed by roasting at 850–1150 °C to form β-spodumene from α-spodumene [26–28]. The negative Gibbs free energy at this temperature range indicates the formation of reactive and amorphous β-spodumene which helps in the extraction of higher percentages lithium sulfate by the sulfuric acid treatment [26]. The generated lithium slag after the lithium extraction retains sufficient amorphousness and aluminosilicate rich phases to induce pozzolanic reaction as a SCM [29]. Sulfate, chlorine, and carbonate anions of different salts and acids help to recover lithium from β-spodumene, and these negative ions beyond the threshold limit in lithium slag may deteriorate concrete by early cracks, which restrict its high-volume usage as a pozzolan. Therefore, in this study, the pozzolanic activity of low-high volume lithium slag as a SCM will be assessed through portlandite consumption, strength development, and hydration heat.

* Corresponding author.
E-mail address: shaikhfa@rocketmail.com (F.U.A. Shaikh).

https://doi.org/10.1016/j.cemconcomp.2023.105262
Received 25 May 2023; Received in revised form 29 July 2023; Accepted 16 August 2023
Available online 19 August 2023

The reactivity of the pozzolans is usually characterised by the reduction of calcium ions and electrical conductivity in a lime solution [30]. The Ca^{2+} ions in the solution diffuse and are immediately adsorbed onto the pozzolan surface, and the reaction products are formed from the diffused Ca^{2+} ions at pH > 12.0 [31–33]. As more Ca^{2+} ions combine with pozzolan to form hydration products, the pH and electrical conductivity of the unsaturated lime solution decreases with time [31,34–36]. The reactive silica and alumina of pozzolan react with Ca^{2+} ions to form poorly structured calcium silicate hydrate (C–S–H), hydrogarnet (C-A-H) and/or strärtlingite (C-A-S-H) hydration products. The pozzolanic reaction also forms AFt or in combination with AFm phases depending on the availability of sulfate, carbonate, hydroxyl, or chloride ions in the solution [33,37,38]. This study will assess the formation of hydration products of the lime reacted lithium slag on early to extended hydration period through microstructural tests.

Earlier, the pozzolanic activity of lithium slag was calculated from the oxide composition [6] and strength activity index (SAI) [39–41]. Researchers also explained the strength development of the lithium slag concrete products through microstructural assessment, specifically diffraction peaks of crystalline hydration phases [4,42,43] and scanning electron microscopy (SEM) coupled energy dispersive X-ray spectroscopy (EDS) [41,44]. The previous studies left an opportunity to focus on the comprehensive chemical tests to assess lithium slag pozzolanic activity in line with other low-carbon SCMs, and the assessment of amorphous, amorphous intermediate, and crystalline hydration products contributing to strength development and pozzolanic activity. This research investigates, for the first time, the detailed quantification of the pozzolanic activity of lithium slag as a SCM in concrete production through chemical tests and microstructural analysis of hydration products, and comparison with other low-carbon SCMs, thereby contributing to a better understanding of its potential as a sustainable replacement for cement in concrete construction. In this study, lithium slag was characterised through X-ray fluorescence (XRF), X-ray diffraction (XRD), scanning transmission electron microscopy (STEM) coupled EDS, and thermogravimetry (TG). The unsaturated lime and electrical conductivity tests are used as precursor pozzolanic activity tests to determine the reactivity of lithium slag based on the chemical composition, amorphousness, and crystal structure. The optimized percentage 0–60% lithium slag was quantified from Frattini, SAI, and R^3 (rapid, relevant, and reliable) tests. The diffraction patterns and STEM-EDS were used for characterisation of the amorphous and crystalline phases formed by the unsaturated lime reacted lithium slag from early and prolonged hydrations.

2. Materials and methods

2.1. Material characterisation

The physical and chemical properties of lithium slag and cement were investigated in this study. The water content of the received lithium slag was 28.3%. The lithium slag was dried at 105 ± 5 °C temperature for 24 h to remove the moisture and micronized in a traditional ball mill for 10 min at 50 rpm to break the soft agglomerate. The general purpose (GP) cement met the requirements of AS 3972 [45]. The oxide compositions of cement, ground lithium slag, and hydrated lime are shown in Table 1. The major oxides of lithium slag were SiO_2, Al_2O_3, CaO, and SO_3 and their proportions were 54.6%, 21.1%, 7.5%, and 5.6%, respectively.

A Malvern Mastersizer 2000 laser particle analyser was used to determine the grain size distribution of cement and lithium slag in Fraunhofer mode [46], as shown in Fig. 1. The grain size distribution of sand was determined by using the ASTM C778 standard sieves [47]. The median particle size of cement, lithium slag, and sand were 17, 38, and 280 μm, respectively [14]. River sand containing 99% pure crystalline silica was used in the study meeting the requirements of AS 1141 [48]. The hydrated lime was Analytical Reagent (AR) grade containing 95% pure lime, and the calcium carbonate content was less than 1%. The specific gravity of cement, sand, and lithium slag were 3.10, 2.66, and 2.46, respectively [14].

Table 1
Oxide content of cement, ground lithium slag, and hydrated lime[a] (in mass percentage) [14].

Oxides	Cement	Lithium slag	Hydrated lime[a]
SiO_2	20.7	54.6	0.12
Al_2O_3	5.7	21.1	0.08
Fe_2O_3	2.9	1.5	0.05
CaO	63.1	7.5	95
MgO	1.3	0.6	0.6
SO_3	3.3	5.6	<0.10
K_2O	0.4	0.9	–
Na_2O	0.3	0.7	–

[a] Data sourced from manufacturer product data sheet.

The mineral phases of ground lithium slag were determined from the XRD, where 10% corundum (by weight) was used as an internal standard [49]. The diffraction patterns of the materials were recorded using the Bruker D8A with Cu Kα radiation (λ = 1.54056 Å) to detect the minerals in the 2-θ range 5°–120° with a step rate 0.02°/s at 40 kV voltage and 40 mA current. The mineral phases were determined from the ICDD PDF4+ database and TOPAS v.6 was used for the Rietveld refinement. The diffraction patterns and the main crystalline mineral phases of lithium slag and cement are shown in Fig. 2. The relative composition of the crystalline mineral phases of lithium slag were 2.1% β-spodumene ($LiAlSi_2O_6$), 6.6% bassanite ($CaSO_4.0.5H_2O$), 5.4% calcium magnesium carbonate ($Ca_{0.845}Mg_{0.155}(CO_3)$), 23.8% quartz ($SiO_2$), 28.2% anorthite ($CaAl_2Si_2O_8$), 2.3% albite ($NaAlSi_3O_8$), and 31.6% amorphous phase. The amorphous phase in the region 21.8–33° 2-θ contains mostly aluminosilicate composed minerals, as shown in Fig. 2. The presence of carbonate-based minerals in lithium slag are sourced from lithium carbonate production [4]. Similarly, the relative quantification of the mineral phases of cement was determined without using an internal standard [50]. The relative composition of cement minerals were 64% tricalcium silicate (Ca_3SiO_5), 15.2% larnite (Ca_2SiO_4), 9.7% tricalcium aluminate ($Ca_3Al_2O_6$), 6.6% brownmillerite ($Ca_2Al_{0.55}Fe_{1.45}O_5$), 2.6% gypsum ($CaSO_4.2H_2O$), and 1.9% portlandite ($Ca(OH)_2$). The weighted R-factor of Rietveld refinement of lithium slag and cement were 9.14 and 7.7%, this suggest that the curve fitting model provided good approximation in the identification of the mineralogic phases [51].

For STEM imaging, a small quantity of lithium slag powder was ultrasonically dispersed into ethanol, followed by an air drying of the single drop lithium slag dispersion on a carbon-coated specimen grid. A High-angle annular dark-field (HAADF) image and elemental mapping of the lithium slag were generated using the Talos FS200X G2 field emission gun (FEG) STEM coupled Super-X EDS detectors at 200 keV, as shown in Fig. 3(a and b). EDS elemental mapping were analysed in Velox software at selected areas, as shown in Fig. 3(a) of HAADF STEM image. In Fig. 3(a), irregular flaky and angular shaped lithium slag are visible, with a combination of smooth and rough textures. The EDS spectrum on selected area 1 of lithium slag grain shows the presence of silicon, aluminium, calcium, potassium, iron, carbon, and oxygen, as shown in Fig. 3(b). In contrast, the EDS spectrum on selected area 2 shows the presence of calcium, sulphur, and oxygen. The elemental composition of area 2 suggests the presence of bassanite, while a complex formation of different minerals may combine in the agglomerate in area 1. The STEM-EDS and XRF analysis of lithium slag detected notable concentration of iron and potassium. In this study, the XRD analysis of lithium slag cannot accurately distinguish the lithium bearing different micas viz. muscovite ($KAl_2(AlSi_3O_{10})(OH)_2$), lepidolite ($K(Li,Al)_3(AlSi_3O_{10})(O,OH,F)_2$), phlogopite ($KMg_3(AlSi_3O_{10})(OH)_2$), and biotite ($K(Mg,Fe)_3(AlSi_3O_{10})(OH)_2$) [52–54]. The correction applied for the modelling of quantitative XRD phase analysis of lithium slag needed further

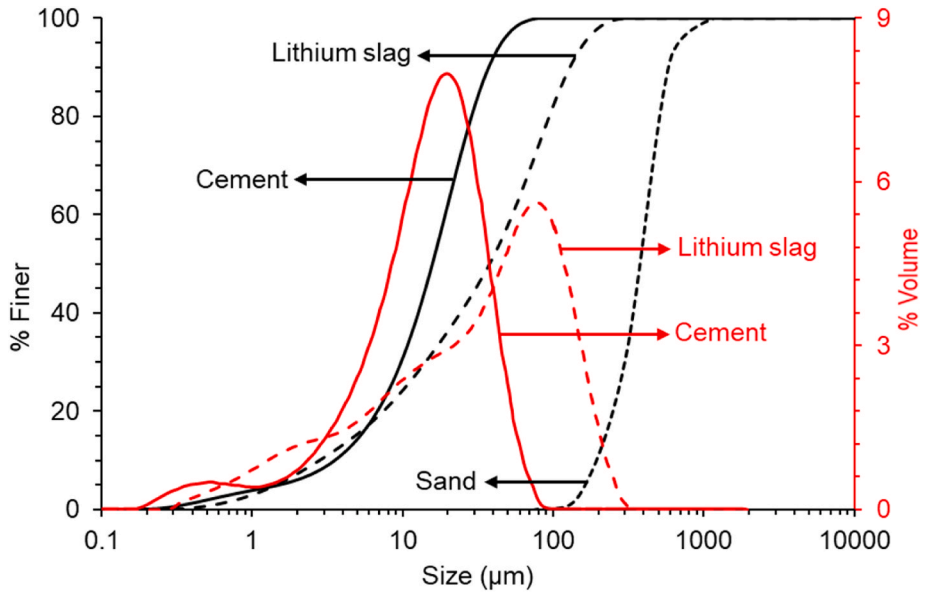

Fig. 1. Grain size and volume distributions of cement and lithium slag through laser particle size analyser. Grain size distribution of sand by traditional sieving.

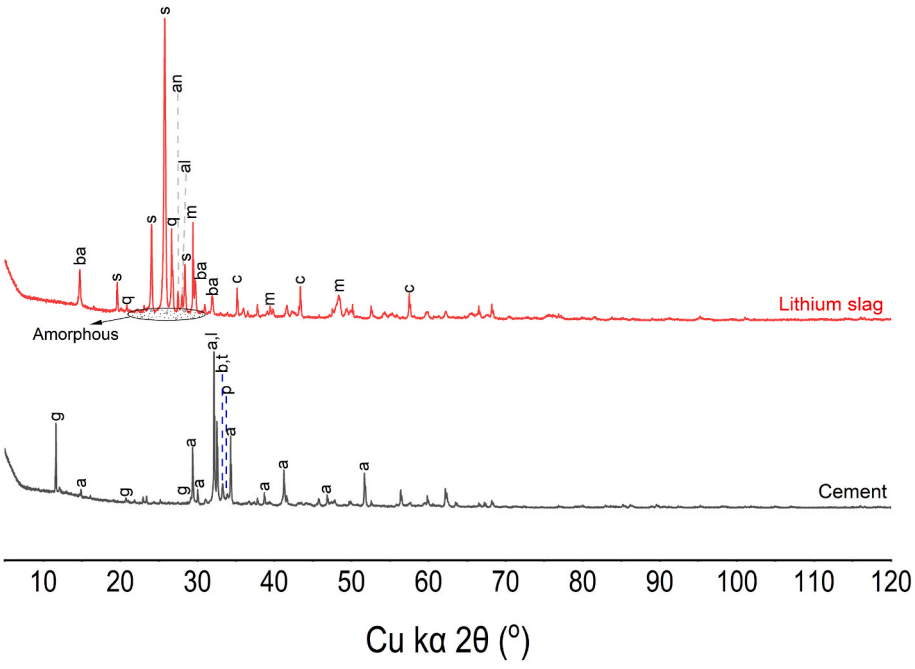

Fig. 2. Diffraction patterns and minerals of cement and lithium slag. The notations of lithium slag minerals are ba, s, q, m, al, an, and c are bassanite (PDF# 00-041-0224), β-spodumene (PDF# 04-016-0110), quartz (PDF# 00-033-1161), calcium magnesium carbonate (PDF# 04-012-6929), albite (PDF# 00-009-0466), anorthite (PDF# 00-012-0301), and corundum (PDF# 04-004-2852), respectively. The notations of cement minerals are g, b, a, p, l, and t are gypsum (PDF# 04-009-1810), brownmillerite (PDF# 04-015-8019), alite (PDF# 04-018-9701), portlandite (PDF# 04-006-9147), larnite (PDF# 04-007-2687), and tricalcium aluminate (PDF# 04-008-8069), respectively.

refinement to get the preferred orientation of the mica crystals [52,55].

The thermogravimetry (TG) of the lithium slag and cement was carried out on SDT Q600 and assessed in accordance with ASTM C1872 [56], as shown in Fig. 4. The mass loss from the room temperature to 170 °C in the TG/DTG curves of lithium slag and cement is caused by the loss of moisture and bassanite water [57,58]. An irreversible conversion of γ-calcium sulfate to β-calcium sulfate occurred at 370–410 °C with a little broad exothermic peak in the cement DTG curve [59]. The mass losses for lithium slag and cement at 400–750 °C were due to the dehydroxylation of the zeolite phases [60] and decomposition of carbonates, respectively [57]. The mass loss of hydroxylated defects of the zeolite phases occurs at ~700 °C, and this reduces the crystallinity of the pozzolans, as detected from XRD [61]. The total mass loss of lithium slag and cement were 8.4% and 2.8%, respectively at 990 °C. In this study, the lithium slag holds 31.6% amorphous phase containing mostly aluminosilicate glassy phases which can contribute to the pozzolanic reaction during hydration of cement particles. Therefore, it is worthwhile to assess the pozzolanic activity of lithium slag through different pozzolanic activity tests.

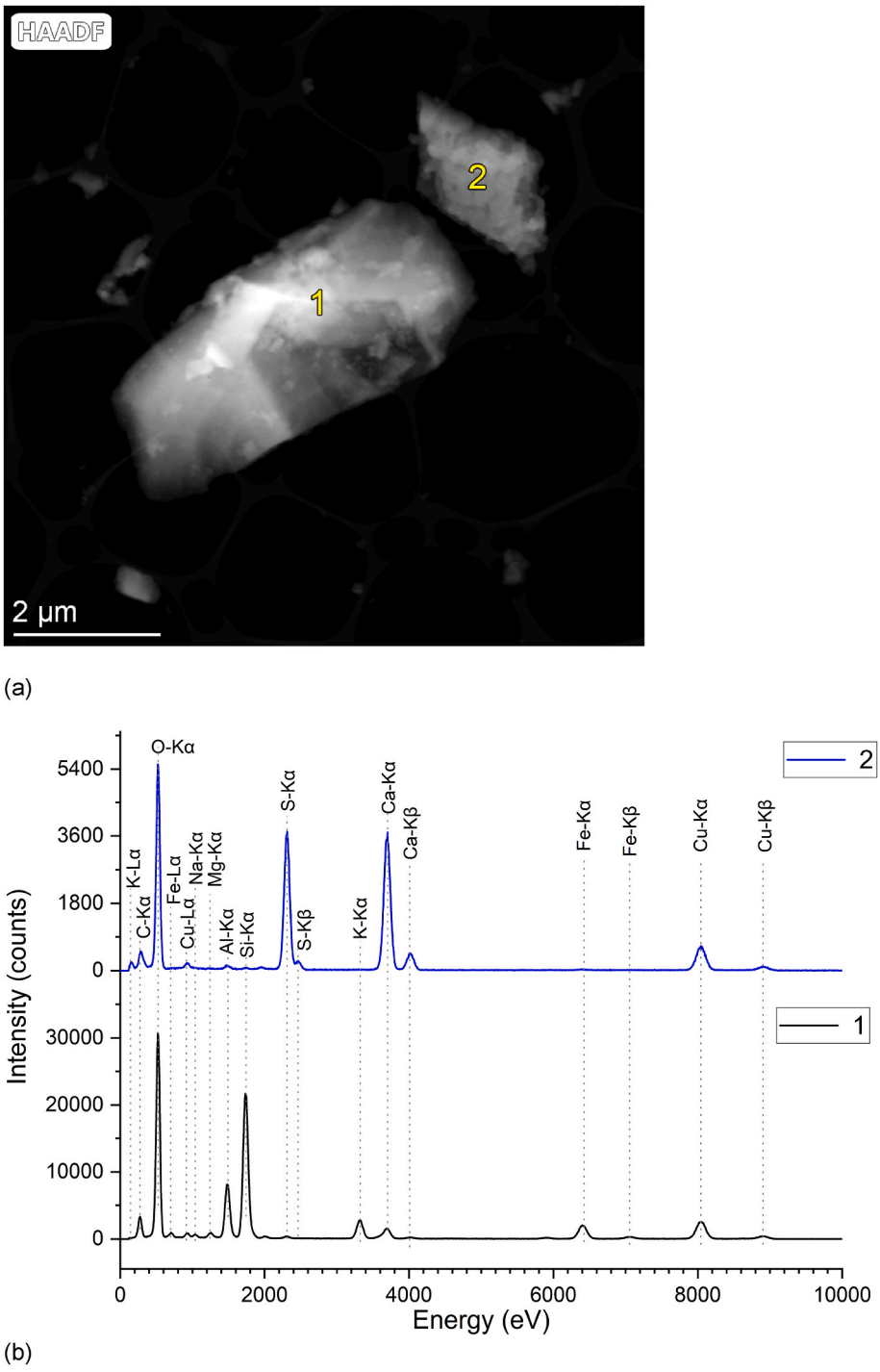

Fig. 3. HAADF-STEM image with locations (area 1 and 2) where EDS spectra were generated (a), and (b) EDS spectra of areas 1 and 2 at 200 keV.

2.2. Experimental methodology

2.2.1. Pozzolanic activity precursor tests

The pozzolanic reactivity of lithium slag was primarily determined from unsaturated lime consumption and electrical conductivity precursor tests. A schematic work hierarchy of the precursor pozzolanic activity tests is represented in Fig. 5. The mix proportions and test ages of the pozzolanic activity tests are shown in Table 2. The unsaturated lime consumption test [32] was conducted by adding 70 mL unsaturated lime solution to 1 g lithium slag at constant 40 °C. An unsaturated lime solution was prepared by adding 1 g pure lime (AR grade) in 1000 mL deionised water for 24 h [36]. The pH and electrical conductivity of the lime solution were 12.38 and 3.82 mS/cm, respectively at 25 °C with nonlinear temperature compensation meeting the requirements of EN 27888 [62]. The samples were vacuum filtered by using Whatman 42, 2.5 μm nominal pore size after 1, 3, 7, and 28 days. The CaO concentration was determined by adjusting the pH of the filtered solution to 12.5 ± 0.2 using 0.1 M HCl, and the alkaline mixture is titrated against 0.03 M EDTA solution using Patton-Reeder's indicator. The CaO concentration was determined by using Eq. (1).

$$[CaO]\ (mmol\,/\,litre) = \frac{1000 \times M_1 \times V_1 \times f_1}{V_2} \quad (1)$$

where, M_1, V_1, V_2, and f_1 are the molarity of EDTA (0.03 M), volume of

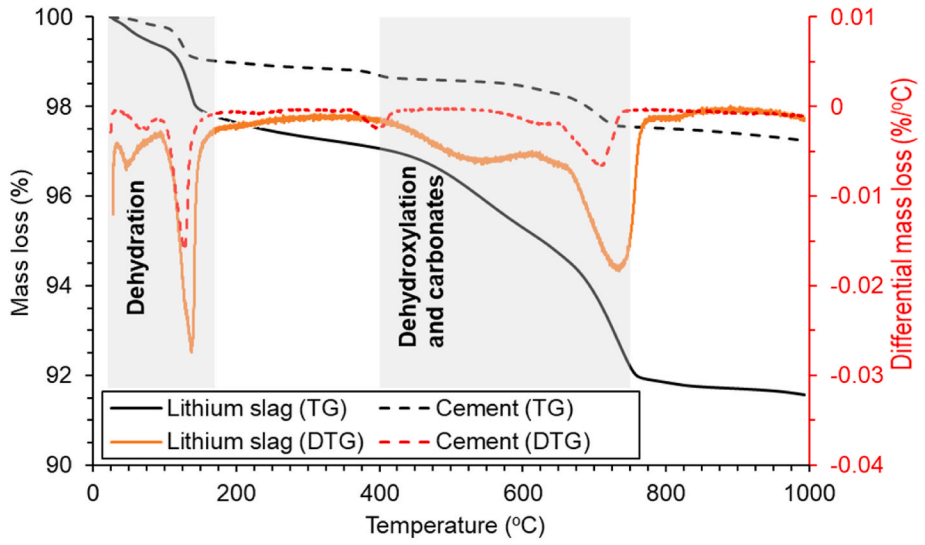

Fig. 4. TG-DTG curves of lithium slag and cement from room temperature to 990 °C. The shaded areas in the TG-DTG curves show the mass loss due to presence of moisture and gypsum, portlandite, and carbonates, respectively.

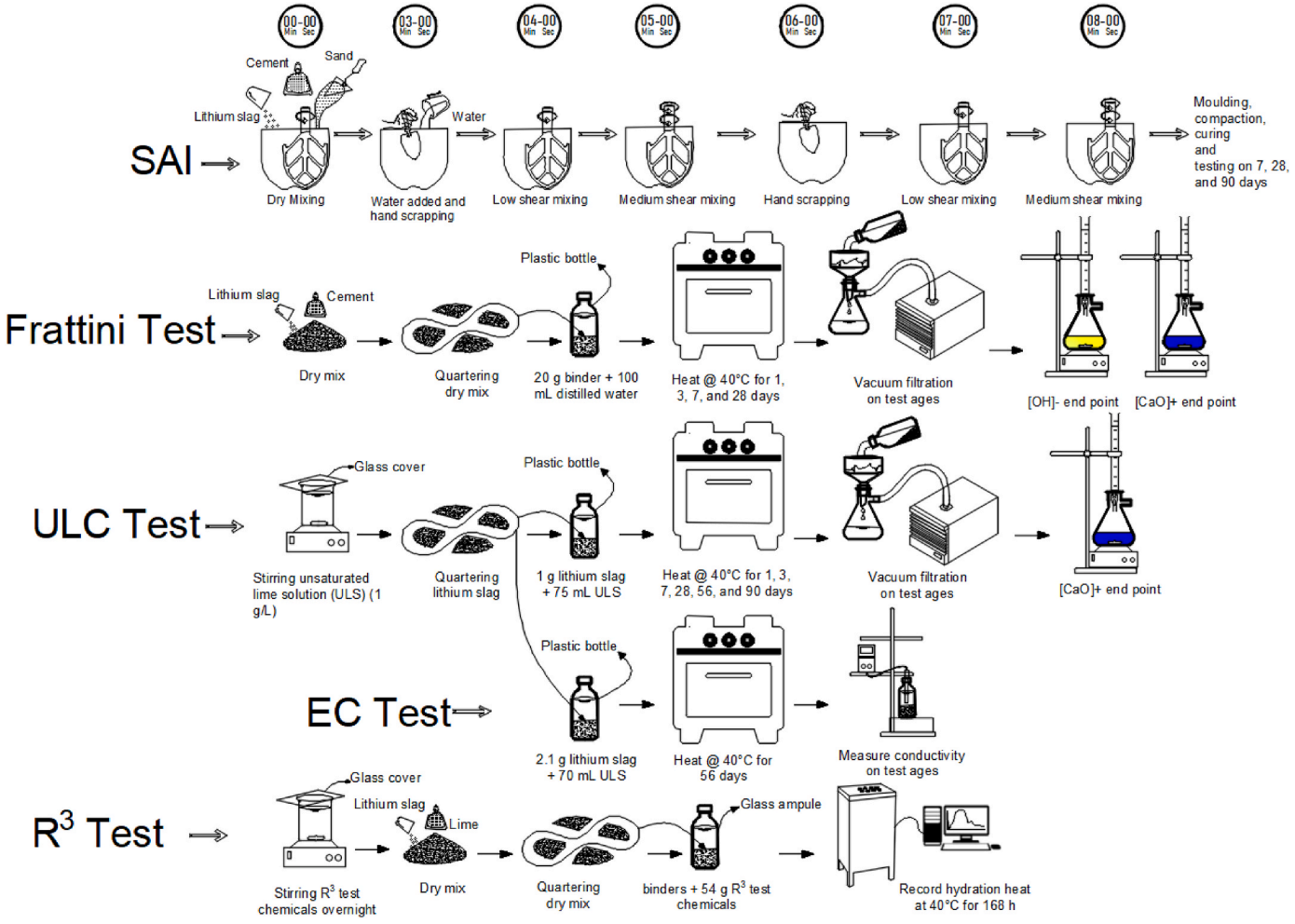

Fig. 5. Schematic representation of the work hierarchy of different pozzolanic activity tests.

Table 2
Mix proportions for different pozzolanic activity tests.

Tests	Mix ID	Cement (g)	Lithium slag (g)	Sand (g)	Water (g)	Time (days)
ULC	–	–	1	–	75[a]	1, 3, 7, 14, and 28
EC	–	–	2.1	–	70[a]	0–56
Frattini	Control	20	0	–	100	1, 3, 7, and 28
	10% LS	18	2			
	20% LS	16	4			
	30% LS	14	6			
	40% LS	12	8			
	50% LS	10	10			
	60% LS	8	12			
SAI	Control	500	0	1375	242	7, 28, and 90
	10% LS	450	50		240	
	20% LS	400	100		242	
	30% LS	350	150		245	
	40% LS	300	200		250	
	50% LS	250	250		255	
	60% LS	200	300		260	

[a] Unsaturated lime solution containing 1 g/L lime in deionised water. Here, ULC and EC stand for unsaturated lime consumption and electrical conductivity, respectively.

EDTA used for the titration in (mL), volume of the filtered solution used for the titration, and normalisation factor for the standardisation of EDTA, respectively.

Later, the electrical conductivity [63] of lithium slag was measured by placing 2.1 g lithium slag in 70 mL unsaturated lime solution (1 g/L) in a sealed polyethylene container. The mixture was slowly rotated and immediately kept in an oven at 40 °C. On the other hand, 2.1 g lithium slag was placed in 70 mL distilled water at same experimental condition [30]. Hach HQ40d conductivity meter (0.01 μS/cm–200 mS/cm at 25 °C) was first calibrated with the manufacturer standard solution. The relative electrical conductivity (C) was determined by Eq. (2), where C_0 and C_t are the initial electrical conductivity and electrical conductivity of at different time durations, respectively.

$$C = \frac{C_0 - C_t}{C_0} \tag{2}$$

2.2.2. Pozzolanic activity tests

In the Frattini test, 20 g of binder weighed (0.0001 g accuracy) and 100 mL deionised water added [64]. Two replica samples were prepared, immediately capped, and kept at 40 °C. The samples were vacuum filtered after 1, 3, 7, and 28 days. The OH^- concentration is determined by adding methyl orange indicator and titrated against 0.1 M HCl solution. The OH^- concentration was determined by using Eq. (3).

$$[OH^-]\ (mmol/litre) = \frac{1000 \times M_2 \times V_3 \times f_2}{V_2} \tag{3}$$

where, f_2, M_2 and V_3 are the normalisation factors for the standardisation of HCl, molarity of HCl (0.1 M), and volume of HCl used for the titration in (mL).

The compressive strength of 50 mm cube mortars was determined by utilizing 10–60% lithium slag as a SCM [65]. The water content of the mixes was determined from the flow diameter of the control specimen ± 5 mm [66,67]. The mixing procedure of the mortar for the SAI test is shown in Fig. 5. The mortar specimens were placed in an unsaturated lime curing bath at 23 ± 2 °C with RH 55 ± 5% followed by an ambient curing for 24 h in a moist room. The compressive strength test was conducted on 7, 28, and 90 days and the SAIs were calculated from Eq. (4) [68].

$$SAI = \frac{compressive\ strength\ of\ the\ moratr\ with\ SCM}{compressive\ strength\ of\ control\ mortar} \tag{4}$$

Table 3
Mix design for R^3 test.

Specimen ID	Lithium slag (g)	$Ca(OH)_2$ (g)	$CaCO_3$ (g)	Potassium solution[a] (g)
10% LS	4	36	5	54
20% LS	8	32	5	54
30% LS	12	28	5	54
40% LS	16	24	5	54
50% LS	20	20	5	54
60% LS	24	16	5	54

[a] The content of potassium solution is 4 g/L KOH and 20 g/L K_2SO_4 in distilled water.

The R^3 test [69–71] was performed to determine the independent reactivity of 10–60% lithium slag used as SCM. The mix proportions of the R^3 test are shown in Table 3. Later, the pure lime (AR grade) and lithium slag were hand mixed with the prepared alkaline solution, and immediately put into the TAM AIR isothermal calorimetry chamber at 40 °C for 7 days. The cumulative heat release from the pozzolan (Q_{SCM}) was calculated from Eq. (5), where Q, m_p, and f are the cumulative heat from 75 min to 168 h, mass of the paste, and mass fraction of SCM in the paste specimen. Later, the bound water of R^3 test pastes was determined from Eq. (6), where m_{c+p}, m_{c+dp}, and m_c are the mass of dried SCM and crucible, mass of heated SCM and crucible, and mass of cooled crucible.

$$Q_{SCM}\left(J/g\ of\ SCM\right) = \frac{Q}{(m_p \times f)} \tag{5}$$

$$Chemically\ bound\ water_{SCM}\left(g/100\ g\ of\ SCM\right) = 100 \times \frac{m_{c+p} - m_{c+dp}}{m_{c+p} - m_c} \tag{6}$$

2.3. Microstructural analysis of unsaturated lime reacted lithium slag

The hydrated phases of lithium slag cement mortars are sensitive to grinding, as the temperature and friction during intense grinding have the possibility of losing crystal water, phase disassemble, and contamination [72,73]. In this study, the reacted lithium slag from the electrical conductivity test was found suitable for the determination of hydrated phases to avoid heavy mechanical micronization [74]. The reaction product was separated by filtration and the hydration was stopped by using isopropanol (solvent exchange method), which was replaced in every 24 h until 3 days and dried at 40 °C for 8 h to dry the sample. The sample was vacuum desiccated for another 72 h [25,73]. The samples were powered and passed through a 75 μm sieve. The diffraction pattern of the reacted ionised samples was recorded by using the Bruker D8D with Co Kα radiation (λ = 1.78899 A°) to detect the hydrated phases of the minerals at 35 kV voltage and 40 mA current [74]. The sample was dispersed in ethanol and droplets were sprayed on the low background

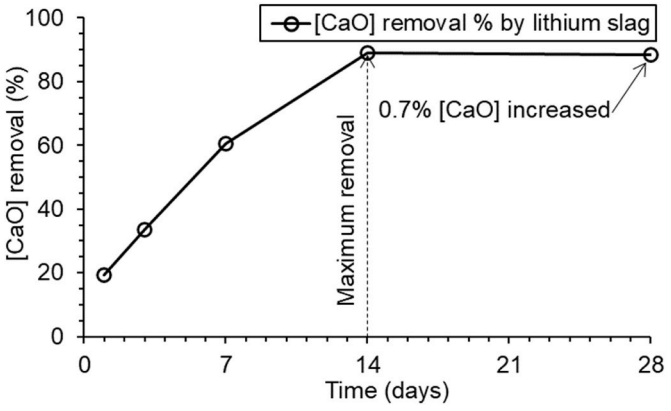

Fig. 6. [CaO] removal % from unsaturated lime solution (1 g/L) by lithium slag at 1, 3, 7, 14, and 28 days for 40 °C.

holder by a dropper. The droplets were air dried, and the diffraction data was collected within 5–35° 2-θ range with a step rate 0.013°/s. The diffraction data was recorded in XRD Wizard software with 0.1 s/step and the total time duration for an analysis was 25 min. The hydrated phases of the reacted samples were determined from Diffrac. eva v.6 software and ICDD PDF4+ database. The STEM coupled EDS of the lime reacted lithium slag after the electrical conductivity test was performed as detailed earlier.

3. Results and discussions

3.1. Pozzolanic activity precursor tests

3.1.1. Unsaturated lime consumption

Fig. 6 shows the percentage reduction of CaO concentration from the fixed lime (1 g/L) solution at 40 °C by lithium slag on 1, 3, 7, 14, and 28 days. For the assessment of the pozzolanic activity of lithium slag, 1 g/L unsaturated lime solution was prepared in this study to minimize the potential shortcoming that 2 g/L lime does not completely dissolve [33]. A saturated lime solution prepared from 2 g/L $Ca(OH)_2$ in deionised water exceeded the lime solubility and the excess lime retained on the filter paper that increased the residual lime concentration of a pozzolan [33]. In Fig. 6, the lithium slag is highly efficient in consuming 19.4% lime in one day, followed by 33.5% and 60.4% lime removal on 3 and 7 days, respectively. The efficiency of lime removal slightly reduced after 7 days, and 28.5% lime was removed by lithium slag from 7 to 14 days. Lithium slag was able to exhibit 889 mg $Ca(OH)_2$/g pozzolanic activity at 31.6% amorphous content, and fulfills the pozzolanic activity requirement of BS 8615-1 [75]. However, the pozzolanic reaction further slowed after 14 days. The reduction of Ca^{2+} ions from the solution lead to the reduction of pH, and therefore the pozzolanic reaction slowed down. A small concentration of lime (0.7%) was increased in solution on 28 days, and this may be due to the atmospheric CO_2 inside the capped plastic bottles that may precipitated $CaCO_3$ by reacting with portlandite in the prolonged test duration [31,33,76]. In addition, the soluble alkali metal ions (Na^+, K^+, Mg^{2+}, etc.) from the amorphous minerals of lithium slag may substitute calcium from the pore solution of aluminosilicate phases in near neutral and basic solutions [77]. Therefore, the Ca^{2+} substitution may slightly reduce the lime removal efficiency. A further discussion of this phenomenon is presented in later sections.

Walker and Pavia et al. [30] determined the lime consumed by PFA, micro silica (MS), red brick dust (RBD), ground tile (GT), and yellow brick dust (YBD), and their normalised lime removal capacities were 6.5, 4.7, 19.2, 12.3, and 20%, respectively. The data from different studies were normalised based on test duration, concentration of saturated lime solution, and mass of pozzolan. Additionally, Donatello et al. [33] mentioned that the normalised lime consumption of MK, SF, and PFA were 15.3, 6.5, and 6.4% respectively. Also, Li et al. [78] determined the lime consumption of raw and ground circulating fluidised bed (CFB) fly ashes (FA) and the normalised lime consumption were 10.4 and 11.7%, respectively. Based on the above discussion, the normalised lime consumption of SF, PFA, and MS were low (<10%), followed by raw CFB-FA, ground CFB-FA, and GT were found moderate (10–15%), and MK, RBD, and YBD were high (>15%). In this study, the normalised lime removal capacity of lithium slag was 6.3%, as insufficient Ca^{2+} ions in the unsaturated lime solution could not form much hydration products [33,35].

3.1.2. Electrical conductivity

The reduction of the electrical conductivity in an unsaturated lime solution represents the degree of pozzolanic activity of the SCM in an alkaline medium. The minerals of lithium slag react with available Ca^{2+} and OH^- ions in the unsaturated lime solution, and the reduction of the electrical conductivity slows down with the alkalinity. The variation of electrical conductivity of lithium slag in an unsaturated lime solution (1 g/L) at different time intervals at 40 °C is shown in Fig. 7. The electrical conductivity of lithium slag in 1 g/L unsaturated lime solution provided a significant understanding of the formation of hydration products. A conductivity rise of 1444 μS/cm was recorded at 120 s after the placement of lithium slag in the deionised water. Therefore, the electrical conductivity of lithium slag in distilled water versus time was plotted in Fig. 7 to indicate the conductivity contribution by the soluble salts of lithium slag. Finally, the theoretical electrical conductivity is plotted in

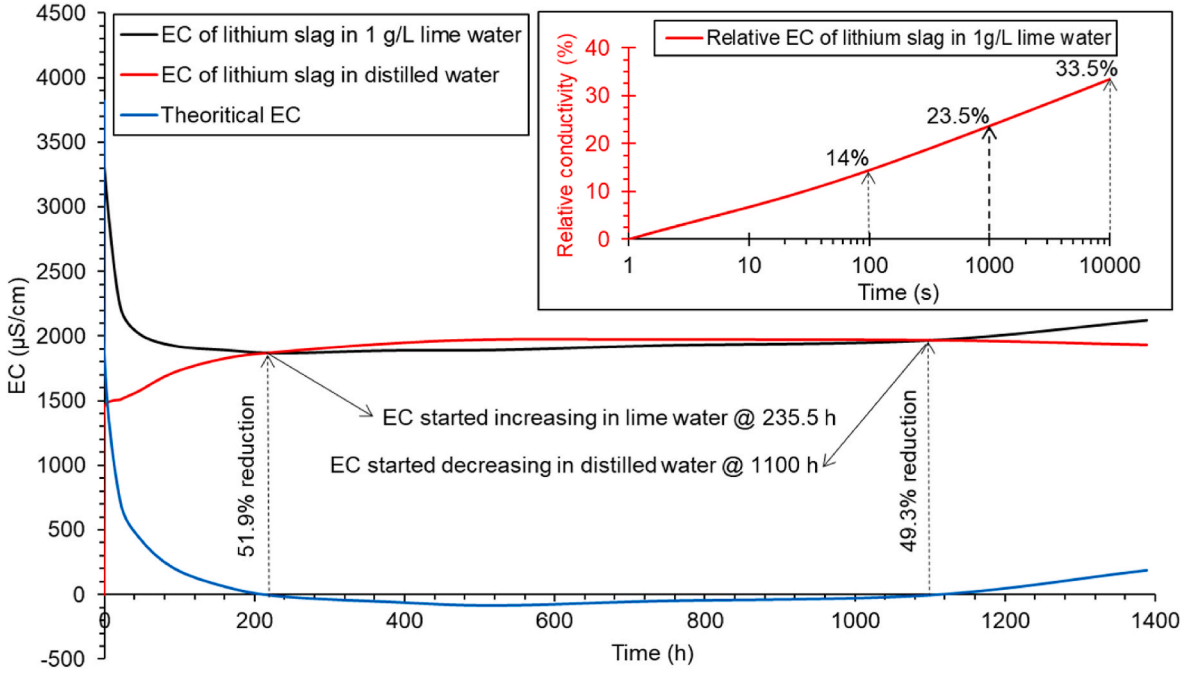

Fig. 7. Variation of electrical conductivity of the lithium slag in unsaturated lime solution (1 g/L) with time. The variation of relative electrical conductivity of lithium slag with time (red coloured line plot). Here, EC stands for electrical conductivity. (For interpretation of the references to colour in this figure legend, the reader is referred to the Web version of this article.)

Fig. 7 from the difference in the electrical conductivity of lithium slag in lime and deionised water. A positive theoretical conductivity indicates the state of reaction of lithium slag with CaO, while a value close to zero indicates the reaction equilibrium.

At an early stage, the electrical conductivity of lithium slag decreased rapidly with time. At 235.5 h, the electrical conductivity of the concentrated lime solution was reduced by 51.9% to initial, followed by a 2.6% increase till 56 days. This clearly suggests that the pozzolanic reaction slowed down at 235.5 h, as Ca^{2+} and OH^{-} ions were highly reduced from the unsaturated lime solution, and some unreacted pozzolans were left to continue the pozzolanic reaction. Particularly, a higher concentration of CaO in the unsaturated lime solution was required to continue the pozzolanic reaction for further reduction in the electrical conductivity [33,35]. The susceptibility of increasing residual lime concentration of pozzolan restricts the use of higher lime concentrated solution for electrical conductivity test [33]. Lithium slag showed a steady electrical conductivity increase in both unsaturated lime and distilled water till 1100 h, as the ion dissolution from the salts of lithium slag continued to add electrical conductivity. In this study, a negligible negative theoretical electrical conductivity was recorded from 235.5 h till 1100 h, and the average maximum negative value was 81 μS/cm at 521.7 h (2.1% of the maximum electrical conductivity). This was probably due to the differences in the ion concentrations of lithium slag used in unsaturated lime and deionised water, which could not be avoided after the sample quartering procedure. At this stage, the reaction between lithium slag and unsaturated lime solution obviously attained equilibrium and the soluble alkali metal ions were probably initiate to deplete Ca^{2+} ions from the pozzolan surface [77,79]. Later, the electrical conductivity of lithium slag in deionised water was slightly decreased after 1100 h, and this may be due to the adsorption of heavy metal ions (Cr^{3+}, Fe^{3+}, etc.) on the pozzolan surface from ionic solution at low pH [80,81]. Thus, the theoretical electrical conductivity turned positive again that steadily increased to 190 μS/cm till 56 days. This indicated that a slow pozzolanic reaction was induced after 1100 h, as some alkali metals could form hydration products with calcium aluminosilicate at low pH. The adsorption of heavy metals on the pozzolan surface is only possible after the precipitation of sufficient hydration products, and higher removal of Ca^{2+} and Al^{3+} ions from the solution [82].

The variation in volume and alkalinity of the unsaturated solution, mass of pozzolan, and temperature affects the rate of reduction of the electrical conductivity of the solution [34,36]. Luxán et al. [34] categorised the pozzolanic material based on the change in electrical conductivity within 2 min. The mass of lime, mass of pozzolan, and volume of water in the unsaturated solution were used as the normalisation parameters. The pozzolans are characterised as non-pozzolanic, variable and good pozzolanic when the normalised reduction in the electrical conductivity are $<2.29 \times 10^{-4}$, $2.29 \times 10^{-4} - 6.86 \times 10^{-4}$, and $>6.86 \times 10^{-4}$, respectively. In this study, the normalised reduction in the electrical conductivity of lithium slag was 3.31×10^{-4} at 2 min, and therefore lithium slag showed a variable pozzolanicity based on Luxán et al. [34] pozzolan classification. The relative conductivity of lithium slag in 1 g/L unsaturated lime solution was calculated and plotted as a line (red coloured) chart in Fig. 7. The rate of increase in the relative conductivity was moderate till 10^2 s and 10^3 s. Later, the relative conductivity rapidly increased till 10^4 s. The relative conductivity of lithium slag with unsaturated lime solution at 10^2, 10^3, and 10^4 s were 14, 23.5, and 33.5%, respectively. Payá et al. [36] investigated the electrical conductivity of nine different sources of low calcium fly ash at 40 °C whose median SiO_2+Al_2O_3+Fe_2O_3 and Blaine fineness were 82.3% and 249 m^2/kg, respectively. The median values of the relative conductivity of the pozzolans at 10^2, 10^3, and 10^4 s were 9.4%, 14.44%, and 20.18%, respectively at 40 °C. Lithium slag and low calcium fly ash both had a slow increase in the relative conductivity till 10^3 s, but lithium slag speeded up in increasing the relative conductivity from 10^3 to 10^4 s, and this was higher in the same comparison [36]. On the other hand, the relative conductivity of high calcium fly ash [36], metakaolin [83,84], and volcanic ash [85] were reported higher than the low calcium pozzolans at 10^3–10^4 s at 40 °C.

The results of precursor pozzolanic activity tests on lithium slag are simple but effective for understanding the generic behaviour of lithium slag as a pozzolan. However, a rigorous application of Frattini, SAI, and R^3 tests are required to determine the pozzolanic activity of lithium slag and its maximum utilisation as a low carbon SCM by optimising hydration heat, strength, and microstructure.

3.2. Pozzolanic activity of 0–60% LS

3.2.1. Frattini test

The unreacted concentrations of CaO and alkalinity of an aqueous cement-SCM mixture (w/b = 5) were determined through titrations and compared with lime solubility at the same alkalinity at 40 °C [64]. A cement-SCM mixture is considered pozzolanic when the lime concentration at a measured alkalinity in the suspension is less than the saturated lime concentration at that alkalinity. In Fig. 8, the data points above and below the lime solubility curve are characterised as non-pozzolanic and pozzolanic systems, respectively.

The calcium and hydroxyl concentrations of 0–60% LS pastes' suspension solution were determined on 1, 3, 7, and 28 days at 40 °C, and the data points are shown as a scatter plot in Fig. 8. The initial hydroxyl concentration of the control sample was greater than 57.5 mmoL/l (pH > 12.76) and suitable to continue the pozzolanic reaction [33]. In this study, 0–40% LS pastes were characterised as non-pozzolanic systems in 1 day, and interestingly, 50–60% LS pastes were found as pozzolanic mixtures. From Table 1, the theoretical CaO concentration in Frattini test specimens for control, 50% and 60% LS mixes are 126 g/L, 70.6 g/L, and 59.5 g/L, respectively. The calcium concentration and alkalinity of 50–60% LS pastes in the suspension solution were highly decreased, but a slight increase in the alkalinity was provided by Na^{+}, K^{+}, and Mg^{2+} ions of cement clinker and pozzolan [33]. Hence, at the same alkalinity, the theoretical lime concentration became higher for 50–60% LS pastes, while experimentally determined calcium concentrations were lower and 50–60% LS pastes were pozzolanic. As expected, the lime concentrations of 0–60% LS pastes were decreased gradually on 3, 7, and 28 days and all mixes were characterised as a pozzolanic system. Also, the alkalinity of the solution degraded with time, as the calcium ions in the suspension solution reacted with SCM to form hydration products. The Frattini test was unable to characterise the pozzolanic and non-pozzolanic mixtures for high volume lithium slag pastes and this is a major shortcoming after the poor interlaboratory reproducibility (average coefficient of variation is 73%) [71,86]. Most researchers used 20% pozzolan (by wt.%) as a SCM in Frattini test, and found metakaolin (MK), silica fume (SF), pulverised fuel ash (PFA), bentonite, and kaolin were pozzolanic [33,87–89]. In this study, an increase of the SCM percentage diluted the clicker and reduced the total lime content in the mixes. The 0–60% LS pastes produced a contradictory result to characterise the pozzolanic mixes, as 50–60% LS pastes became pozzolanic in 1 day. Apart from the Frattini test, the relative reduction percentage of the CaO concentrations can be calculated to characterise the reactivity of 0–60% LS pastes on 1–3, 3–7, and 7–28 days. A relative percentage decrease in the CaO concentration of 0–60% LS pastes on 1–3, 3–7, and 7–28 d is shown as a bar diagram in Fig. 8. The relative decrease in the CaO concentrations of 30–60% LS are extremely low on 1–3 days and the pozzolanic activity of the mixes may be dormant at this

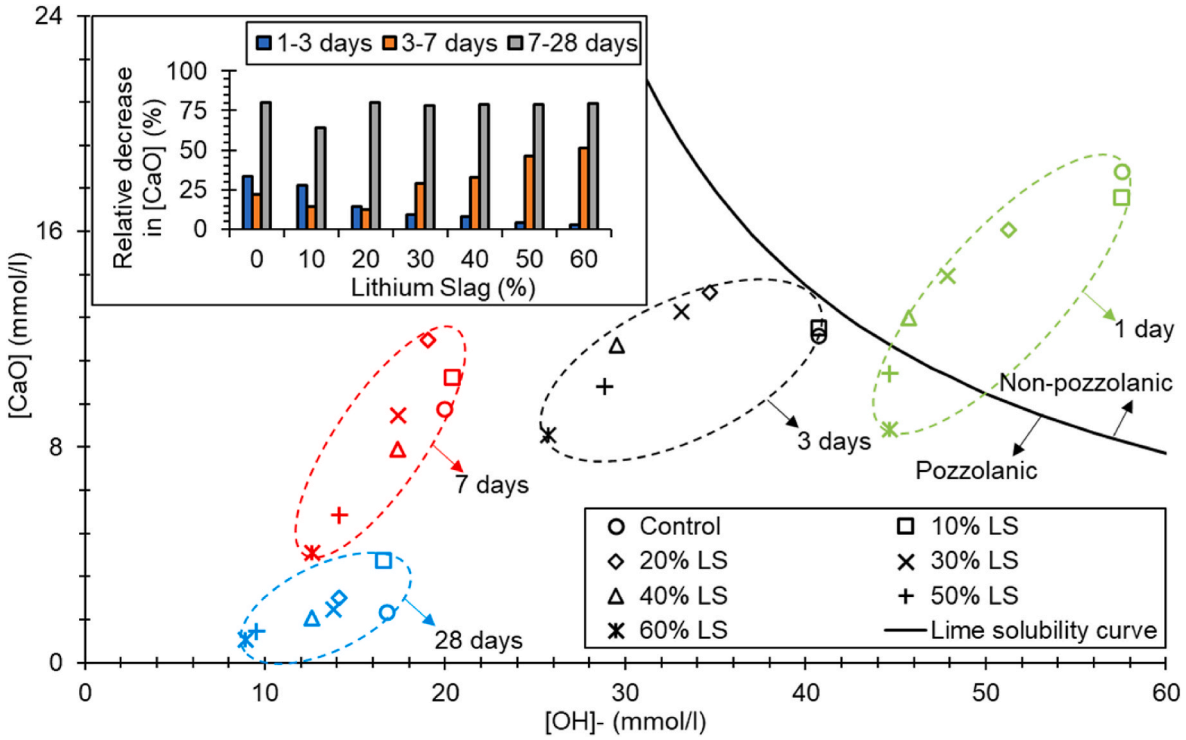

Fig. 8. Change in concentration of [CaO] versus $[OH]^-$ on 1, 3, 7, and 28 days for 0–60% LS pastes (w/b = 5) through Frattini test at 40 °C. The equation of the lime solubility curve is expressed as $[CaO]_{max} = \frac{350}{[OH]-15}$ [33,64]. The bar diagram represents the relative reduction of the CaO concentration of 0–60% LS pastes on 1–3, 3–7, and 7–28 days.

stage. The hydraulic activity of 30–60% LS pastes is accelerated at 3–7 days and the lime removal from the saturated solution is faster, followed by a stable stage at 7–28 days. Thus, pozzolanic activity of lithium slag initiated after 3 days, as the glassy aluminosilicate amorphous phase reacted with the pore solution of cement pastes in alkaline condition [90]. The relative decrease in CaO concertation at 3–7 days proportionally increased with the amorphous phase percentage of the mixes, therefore the alkali metals in the amorphous phases of lithium slag obviously started reacting with calcium and aluminosilicate phases to form amorphous hydration products [91–97]. Later, the calcium removal was stabilised at 79% for 20–60% LS pastes at 7–28 days, as maximum calcium ions were removed from the saturated solution.

3.2.2. *Strength activity index (SAI)*

The compressive strength and average SAIs of 0–60% LS mortars are presented in Fig. 9. The error bars in the bar chart indicated the

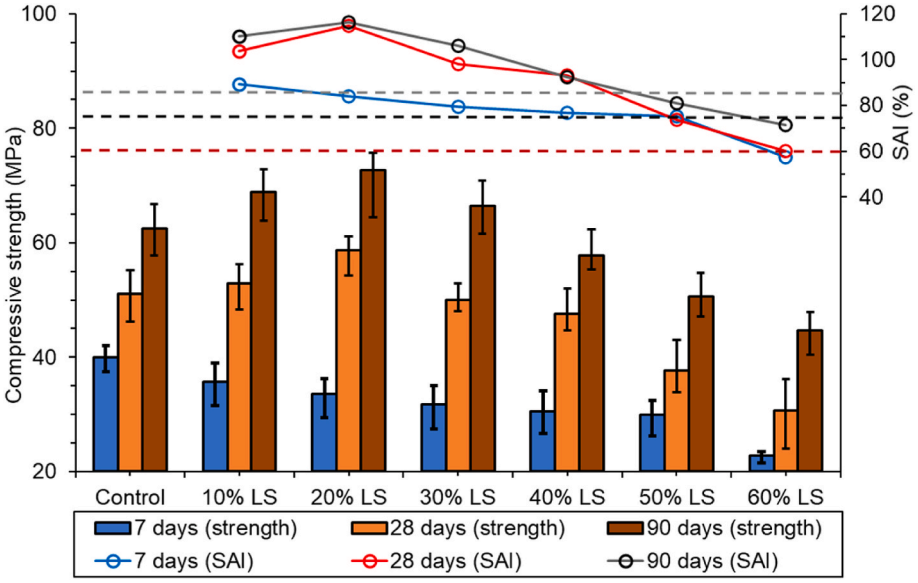

Fig. 9. Compressive strengths and average SAIs of 0–60% LS mortars on 7, 28, and 90 days. The top, middle, and bottom dash lines indicated the strength requirement of the mortars for 85% (EN 450-1 [98] for 90 days), 75% (ASTM C618 [66] for 7 and 28 days; EN 450-1 [98] for 28 days) and 65% (RILEM TC 267-TRM phase 3 [99] for 28 days) SAIs.

maximum and minimum compressive strength of the 0–60% LS mortars. The mix design of 0–60% LS mortars is shown in Table 2. The w/b ratio of the mortars was determined by the flowability requirements specified by ASTM C1437 [67]. The mortar flow of the mixes was kept within ±5 mm of the control and the flow diameter was determined. The w/b ratio of 10–20% LS mortars was equal to the control followed by an increasing trend for 30–60% LS mortars as shown in Table 2. The flow diameter of the fresh control mortar was 232 mm. The water demand for 30–60% LS mortars (greater than 25% SCM by ASTM) was higher than the control mix, limiting the requirement of workability.

The 7 and 28 days compressive strength of the control were 39.9 and 51.1 MPa, respectively. Although the amorphous phase content of 0–60% LS mixes was increased, the 7 days strength development of the 0–60% LS pastes consistently decreased due to lack of sufficient clinker in the system to form amorphous hydration products. The 28 days compressive strength of 10–20% LS mortars was increased compared to the control, followed by a consistent strength reduction for rest of the mixes. The maximum 7 and 28 days SAI were 89% and 115% for 10% and 20% LS, respectively, while 60% LS produced the lowest SAI (57% and 60%) in the same comparison. As lithium slag is a new SCM, the compressive strength test of the 0–60% LS mortars was extended to 90 days. Inert and slowly reactive SCMs can be pozzolanically active after 28 days and screening inert, moderate, and high reactive systems from 0 to 60% LS mortars can be easily comparable [71]. The development of SAI of 0–60% LS mortars was slightly higher on 90 days than the 28 days. The 20% LS mortar produced the maximum SAI was at 116%, followed by the 10% LS mortar at 110% at 90 days. A maximum of 40% LS could gain 77% SAI to qualify the minimum 7 days SAI requirement [66,99], and also met EN 450-1 [98] requirements at 28 and 90 days with 93% and 92% SAIs, respectively.

A 75% SAI requirement at both 7 and 28 days compressive strength tests was set by ASTM C618 [66]. In this study, 10–50% LS mortars met the 7 and 28 days SAI requirements. On the other hand, EN 450-1 [98] requires a minimum of 75% and 85% SAIs at 28 and 90 days, respectively. A 10–50% LS mortars met the EN requirement of SAI at 28 days as shown in Fig. 9, while The SAIs of 10–40% LS mortars passes at 90 days. Based on ASTM and EN standards threshold requirements, a 40% LS mortar is found to have sufficient SAI at 7, 28, and 90 days. RILEM TC 267-TRM phase 3 [99] categorised the reactivity of pozzolans based on the SAI, where non-reactive, moderately reactive, and highly reactive pozzolans were classified when SAIs are less than 65%, 65–100%, and more than 100%, respectively at 28 days. Based on RILEM TC 267-TRM phase 3 [99], 10–40% LS mortars were found to be highly reactive systems at both 28 and 90 days, while 20–50% LS were moderately reactive at 7 days. Besides, the SAI of 60% LS paste was found unreactive at 7 and 28 days but became moderately pozzolanic at 90 days. RILEM TC 267-TRM phase 3 [99] was found to be effective in classifying different percentage of SCM contained systems, which extends the SAI requirements specified by ASTM and BS standards.

3.2.3. R^3 test

The chemicals used for the R^3 test provide a highly alkaline system which facilitates the SCM to combine with the portlandite to continue the pozzolanic reaction. The hydration products formed by the pozzolanic reaction produce significant heat [71,100]. The amount of heat released in the R^3 test is related to the formation of hydration products and bound water. Fig. 10(a and b) shows the heat rate and cumulative heat released per g of SCM of 10–60% LS pastes. As expected, the heat rate and cumulative heat continued to reduce with the increase of lithium slag content in the R^3 test mix. From Fig. 10(a), the hydration heat rate of R^3 test mixes showed distinct phases that can be categorised

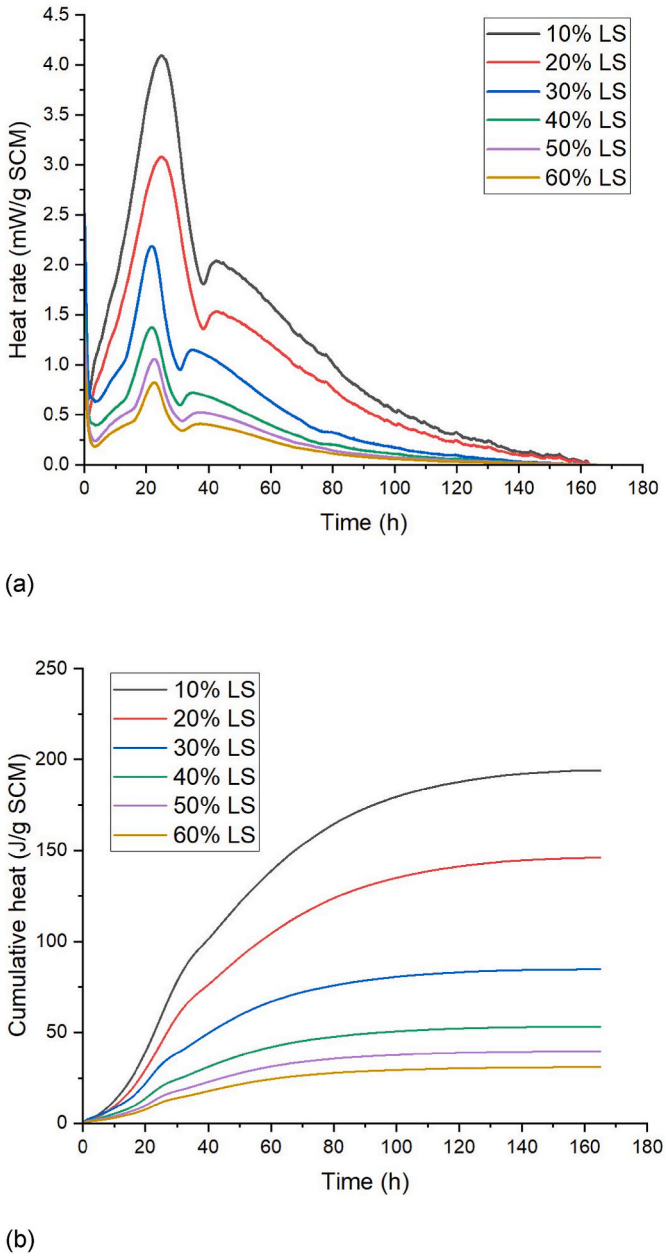

Fig. 10. Isothermal calorimetric analysis of R^3 test pastes: (a) heat rate versus time, and (b) cumulative heat versus time.

into four regions. Firstly, a high heat burst was observed within 15–20 min of mixing dry materials in the alkaline water. The dry binders dissipate a high amount of heat for a short duration due to wetting and dissolution in water followed by a dormant period [101–103]. Secondly, the formation of AFt is induced in the dormant period at 3–4 h due to the dissolution of reactive SO_4^{2-}, Al^{3+}, and CO_3^{2-} ions [104]. The dormant period was slightly delayed for 30–60% LS pastes than the 10–20% LS. Thirdly, the dormant phase is accelerated by amorphous silicate phases of the pozzolan and portlandite to form C–S–H, C-A-S-H or N-(C)-A-S-H at 20–22 h of hydration followed by a deacceleration of hydration heat [101–104]. The dissolved alumina and bassanite of the pozzolan in presence of the lime in the solution controls the induction period [105]. In this study, the primary hydration peaks of 30–60% LS were slightly

delayed compared to the 10–20% LS pastes. Also, the hydration heat rate in the accelerating phase was consistently reduced with the increase of lithium slag content in the R^3 test mix proportion. In the deacceleration phase, the AFt reacts with the available sulfate and carbonate to produce the AFm phase, and a second hydration heat peak occurred at 30–44 h. The 30–60% LS pastes had a higher sulfate content than the 10–20% LS, therefore the deacceleration phase was shifted left by 9–10 h.

In Fig. 10 (b), the total hydration heat produced in the R^3 test by 10–60% LS pastes were 194, 146, 84.6, 53.1, 39.7, and 30.9 J/g SCM, respectively. Kalina et al. [106] classified the pozzolan reactivity based on the hydration heat generated by the R^3 test at 40 °C. A SCM was considered highly pozzolanic, moderately pozzolanic, and inert when the cumulative hydration heat is more than 200, 100–200, and less than 100 J/g SCM, respectively [106]. The total hydration heat of 30–60% LS pastes was less than 100 J/g SCM, and the systems can be classified as inert. In contrast, the total hydration heat of 10–20% LS pastes was in between 100 and 200, and similarly, the mixes can be categorised into moderately pozzolanic. Based on the above discussion, 30–60% LS mixes were unable to produce required hydration heat to be used as a SCM. Later, RILEM TC 267-TRM phase 3 [99] classified different SCMs and the study specified the range of the cumulative hydration heat for natural pozzolan was 50–300 J/g SCM. In this study, the total hydration heat produced by 50–60% LS mixes was less than the threshold hydration heat requirement by the natural pozzolan. The bound water content of 7 days R^3 test 10–60% LS specimens were 6.69, 6.36, 5.73, 4.99, 4.49, and 4.35 g/100 g of dry paste, respectively. The bound water content of 10–40% LS pastes met the requirements for natural pozzolans (4.5–8.3 g/100 g dry paste) [99].

4. Microstructure of hydrated products

4.1. XRD

The XRD analysis of raw and lime reacted lithium slag (at 40 °C) at 1, 3, 7, and 56 days are represented in Fig. 11 (a). The lime reacted lithium slag formed early AFt and was found stable from 1 to 7 days at 10.61°, 18.41° and 24.32° 2-θ (Co Kα) as shown in Fig. 11 (b). In general, Bassanite ($CaSO_4.0.5H_2O$) dissolves at 23–37 °C within a minute and forms AFt with available alumina at 1 day [105,107]. The externally added lime and available sulfate and alumina in lithium slag further accelerated the AFt formation at 3 days, followed by consecutive decrease in the XRD peak at 7 and 56 days. The diffraction patterns of lime reacted lithium slag detected stable AFm phase monocarboaluminate ($C_4AX_2H_n$, X = OH^-, NO_3^- and, C_4AXH_n, X = SO_4^{2-}, CO_3^{2-}) at 13.56° and 26.75° 2-θ (Co Kα) [74]. In addition, the monocarboaluminate may contain different anion species in a single crystal [108]. At higher lime content, the AFt partially reacts with available soluble sulfate and carbonate to transform into monocarboaluminate [74,109,110]. In R^3 test, the second hydration peak showed AFm formation after 30–42 h, as shown in Fig. 10(a). The AFt and AFm peaks followed a similar trend, and both peaks of both phases lowered at 7 and 56 days. In addition, the formation of C–S–H peak at 34.3° 2-θ (Co Kα) was detected from the XRD patterns [74,111]. The C–S–H peak broadening is visible till 3 days and reduced at both 7 and 56 days, as shown in Fig. 11(c). It was probably because, the soluble alkali metal ions Na^+, K^+, and Mg^{2+} ions from anorthite, albite, spodumene, and magnesium bearing calcite may react with C–S–H to form amorphous phases, and therefore, the diffraction peak of C–S–H reduced at 7 and 56 days [33,74]. The reactive alkali metals in the amorphous phase of lithium slag attacked the crystalline and semi-crystalline phases and a progressive reduction of AFt, AFm, and C–S–H occurred after 3 days [112] and showed a consistent trend of CaO removal discussed in earlier sections. The formation of amorphous phases reduces gel and capillary pores, and therefore provides consistent strength development from 7 to 90 days [111]. A further discussion on

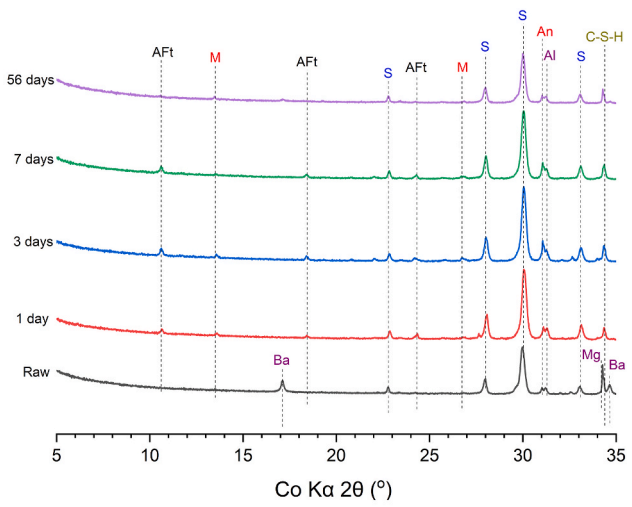

(a)

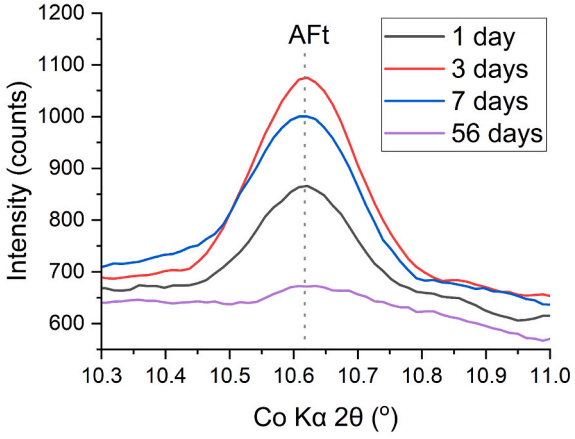

(b)

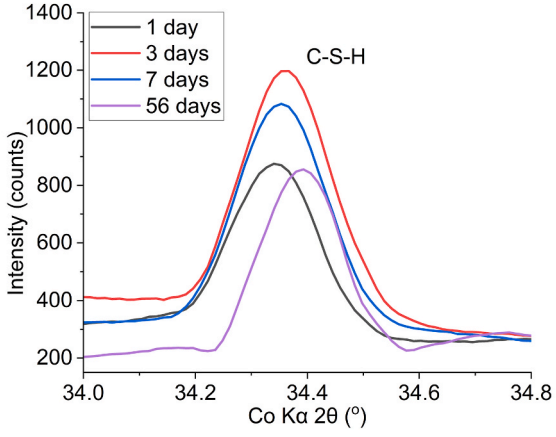

(c)

Fig. 11. Diffraction patterns of unsaturated lime reacted lithium slag after electrical conductivity test (a), ettringite: AFt (b), and (c) C–S–H at 1, 3, 7, and 56 days. Here, AFt, M, Ba, S, An, Al, and Mg notations stand for ettringite, monocarboaluminate, bassanite, β-spodumene, anorthite, albite, and magnesium bearing calcite, respectively.

the formation of hydration products of unsaturated lime reacted lithium slag is presented in section 4.2.

4.2. STEM-EDS

The microstructure of the hydrated phases of unsaturated lime reacted lithium slag was studied in this section. A summary of the hydration products from the reaction of unsaturated lime and lithium slag at 1, 3, 7, and 56 days is shown in Fig. 12. The size fractions of lime reacted lithium slag powder were 1–7 μm, and discretely dispersed in a carbon grid analysed in STEM. A HAADF-STEM image of the 1 day lime reacted lithium slag is shown in Fig. 13(a). The AFt and AFm needles are clearly visible in between the lithium slag agglomerates and are closely held. The EDS was generated at positions 1–4 (Fig. 13(a)), and the spectra are shown in Fig. 13(b).

The AFt are short stubby crystal needles associated with high aluminium peak [113] and the position 3 (Fig. 13(a and b)) indicated the higher peaks of Ca, S, Al, and O, directed the formation of AFt [114].

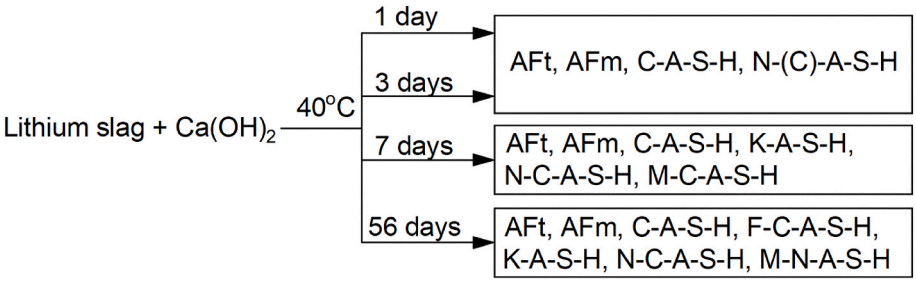

Fig. 12. Summary of the hydration products from unsaturated lime reacted lithium slag at 1, 3, 7, and 56 days.

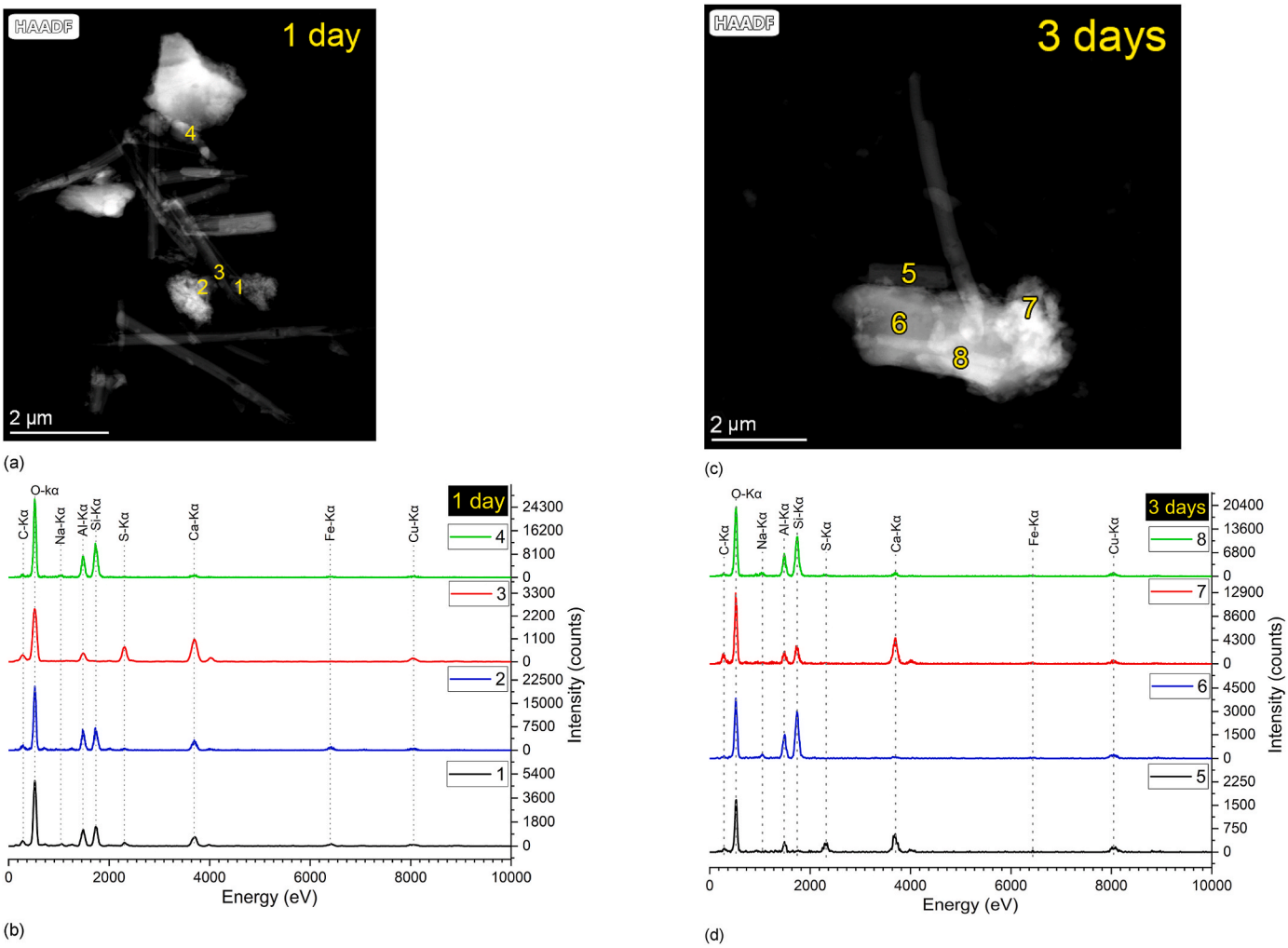

Fig. 13. HAADF STEM images of lithium slag after the electrical conductivity test on 1 day (a), 3 days (c), 7 days (e), and 56 days (g) specimens, and the numeric digits on the images are the selected areas for EDS generation. The EDS spectrum of selected areas 1–4 for 1 day (b), 5–8 for 3 days (d), 9–12 for 7 days (f), and (h) 13–18 for 56 days.

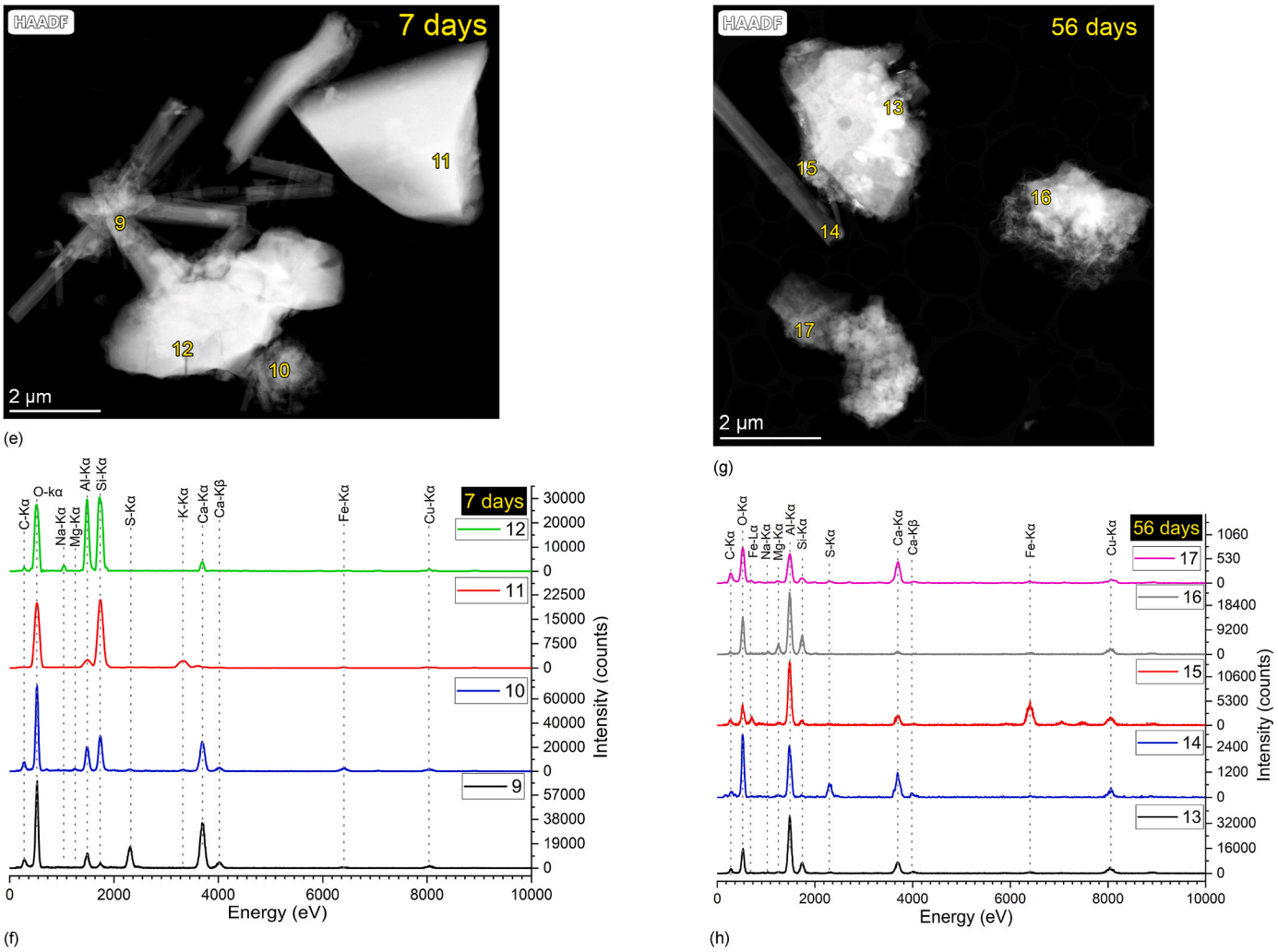

Fig. 13. (*continued*).

A small peak of C-Kα at position 3 (Fig. 13(b)) may form AFm phase monocarboaluminate [110]. The diffraction pattern of lime reacted lithium slag showed that monocarboaluminate is a stable hydration product, and the principal and sandwiched layers of mono-carboaluminate lamellar structure are $[Ca_2(Al)(OH)_6]^+$ and $[0.5X.2.5H_2O]^-$ (X = CO_3^{2-} and SO_4^{2-}), respectively [108]. Here, carbon was associated with higher peaks of Al, Ca, S, and O, which may indicate the formation of monocarboaluminate (Fig. 13(a and b)) [74,108,110]. The Ca-Kα peak in the EDS indicates the degree of calcium reacts with amorphous aluminosilicate phases of lithium slag in positions 1, 2, and 4. The positions 1, 2, and 4 (Fig. 13(a and b)) suggested that the aluminosilicate phase partially, moderately, and insignificantly reacted with unsaturated lime solution. The hydration product of the peaks of Ca, Si, Al, and O indicated the formation of C-A-S-H in 1 day [74,115,116]. Again, a small amount of Na-Kα peak was detected at position 1 and 4, and at high aluminium rich phase sodium reacts poorly structured C–S–H to form amorphous aluminium bearing pectolite N-(C)-A-S-H at 1 day [117–119]. The porosity of N-(C)-A-S-H phase is higher than that of the C-A-S-H, and amorphous or amorphous intermediate phases may form in prolonged hydration, which may reduce the porosity, and induce strength in SCM based concrete products [120].

The lime reacted lithium slag sample was analysed at 3 days, and the EDS was generated at positions 5–8 (Fig. 13(c and d)). The peaks of C, S, Al, Ca, and O at position 5 (Fig. 13(d)) indicated the formation of AFt/AFm phases. The positions 6 and 8 (Fig. 13(c and d)) suggested that sodium was partially reacted with aluminosilicate phase to form N-(C)-A-S-H. The peaks of Ca, Si, and Al at position 7 (Fig. 13(c)) indicated the formation of C-A-S-H. In Frattini test, the relative decrease in CaO from 1 to 3 days was not accelerated (Fig. 8 (bar diagram)), as the alkali metals in the amorphous phase of lithium slag delayed in the formation of hydration products. Therefore, the diffraction pattern of reacted lithium slag showed the maximum intensities of AFt, AFm, and C–S–H at 3 days, as shown in Fig. 11(a–c).

The EDS was generated at positions 9–12 (Fig. 13(e and f)) of the unsaturated lime reacted lithium slag at 7 days. The position 9 (Fig. 13 (f)) on the crystal associated with higher Al, C, Ca, S, and O peaks indicated the formation of AFt/AFm phases [110]. The peaks of Na, Ca, Al, Si, and O at position 12 (Fig. 13(e and f)) indicated the formation of N-(C)-A-S-H. Moreover, at 7 days, the dormant peaks of Mg-Kα and K-Kα at positions 10 and 11 (Fig. 13(f)) may form the amorphous intermediate

M-C-A-S-H [91–94] and K-A-S-H [95–97,118] at low pH. The Mg-Kα peak at position 10 (Fig. 13(e)) indicated that the Mg bearing calcite dissolved in lime solution and at low pH, Mg reacted with C-A-S-H may form M-C-A-S-H hydrates at 7 days [121–123]. Lithium slag reacted with 89% CaO at 7 days, and the electrical conductivity was highly reduced (Fig. 7), thus there is a strong possibility in the formation of amorphous intermediate hydration products M-C-A-S-H and K-A-S-H [97,124]. As a result, the relative decrease in the CaO concentration from 3 to 7 days was accelerated (Fig. 8), and these newly formed amorphous intermediate phases reduced the porosity of N-(C)-A-S-H, and the strength development of lithium slag concrete products was accelerated [91–93,117]. Therefore, the alkali metal ions from the lithium slag amorphous phase attacked the crystalline and partially crystalline phases from 3 to 7 days and formed amorphous and amorphous intermediate hydration products, and consequently the AFt, AFm, and C–S–H diffraction peak was slightly reduced at 7 days than 3 days (Fig. 11(a–c)).

Finally, the positions 13–17 (Fig. 13(g and h)) of unsaturated lime reacted lithium slag at 56 days were analysed by STEM-EDS. The peaks at position 14 (Fig. 13(h)) suggested the formation of AFt/AFm phases, as described for the positions 3, 5, and 9, respectively. The peaks of Ca, Al, Si, and O in the position 13 (Fig. 13(h)) indicated the formation of C-A-S-H phase, as positions 2 and 7. The peaks in position 15 and 16 (Fig. 13(h)) showed an intense Fe-Kα and Mg-Kα, respectively. It was the small concentration of iron sourced from mica minerals of lithium slag that partially substituted silicon to form C-A-F-S-H at extended hydration at position 15 (Fig. 13(g)) [121–123]. The change in the electrical conductivity of lithium slag at 1100 h (Fig. 7) indicated that iron was adsorbed on the pozzolan surface at low pH, and this supported the formation of amorphous intermediate C-A-F-S-H hydration products which partially substituted calcium at 56 days [118]. The adsorption of iron on the pozzolan surface was concentrated at few locations of lithium slag agglomerates, as shown in Fig. A(d) (appendix). In addition, the Mg-Kα peak at position 16 (Fig. 13(g and h)) indicated that the magnesium bearing calcite dissolved in lime solution, and at low pH, magnesium reacted with A-S-H may form M-A-S-H hydrates at 56 days [91–93,117]. At low pH, the unsaturated lime reacted with aluminium rich sites of pozzolan to form stable C-A-H hydrate at position 17 (Fig. 13(g)) [74,91,116]. The formation of amorphous intermediate hydrated phases in the lime reacted lithium slag at 56 days further reduce the gel and capillary pores [111], and induce the strength development of 10–60% LS mortars at 28 and 90 days, as shown in Fig. 9. Also, the development of crystalline C–S–H diffraction peak at 56 days was highly reduced compared to 7 days (Fig. 11(c)), as some of the hydration products formed amorphous intermediate (intermix C-A-S-H) phases in extended duration of hydration [93]. The STEM-EDS colour mapping of the 1, 3, 7, and 56 days HAADF images are provided in the appendix section, as shown in Fig. A (a-d).6.

5. Further discussion

The physical, chemical, and mechanical properties of lithium slag and its products can be compared with the standard specifications for natural SCMs [66,75] and manufactured SCMs [125], as shown in Table 4. The sum of major oxides along with CaO, MgO, and total alkali content of lithium slag met the major standard requirements. The sulfate content of lithium slag is 5.6% which is slightly higher than the standard requirements [66,75,125]. High sulfate content in lithium slag can trigger an internal sulfate attack in concrete, causing durability issues. However, studies have shown that using low volume lithium slag as a supplementary cementitious material (10–30%) with high SO_3 content does not affect the strength [4,126] and durability [4]. In this study, at 40–60% cement replacement, the excess sulfate is unlikely to attack the remaining C_3A phase of cement due to the lower amount of cement and the filler effect of lithium slag. Also, no significant reduction in strengths was observed in three months, indicating that excess sulfate content does not pose a substantial threat to mechanical and durability properties of composites. The loss of ignition (LOI) of lithium slag at 750 °C was 7.8%. The LOI of lithium slag is slightly higher than the AS 3582.4 [125] and BS 8615-1 [75] conditions but meets the ASTM C618 [66] requirement. The grain size of lithium slag was slightly coarser than the standard compliance, but the 31.6% amorphous phase of lithium slag contributed to the rapid strength development of mortars containing 10–60% lithium slag. A 40% LS mortar were also met the standard [66,75,125] requirements of 7, 28, and 90 days SAIs, and water requirement to have a same flowability of the control.

On the other hand, SAI and R^3 test cumulative hydration heat data were also effective in the characterisation of the reactivity of 0–60% LS pastes. The reactivity of lithium slag in 10–60% LS can be interpreted through RILEM TC 267-TRM phase 3 [99], where SAIs of <65, 65–100, >100% are characterised as non-reactive, moderately reactive, and highly reactive systems, respectively. The R^3 test 7 days cumulative heat generated from 10 to 60% LS pastes can be classified by Kalina et al. [106] proposition viz. <100, 100–200, and >200 J/g SCM are characterised inactive, moderately pozzolanic, and highly pozzolanic systems, respectively. Here, 7, 28, and 90 days SAIs of 10–60% LS versus R^3 test 7 days cumulative hydration heat is shown in Fig. 14. It is seen that, 10–20% LS are moderately reactive and pozzolanic, 30–50% LS are moderately reactive but inactive (failing to produce the required amount of hydration heat), and 60% LS are non-reactive (unable to grain the required amount of strength) and inactive. The probability of the occurrence for 7 days SAI with 7 days R^3 test hydration heat exactly matches with the specification proposed by RILEM TC 267-TRM phase 3 [99]. However, the pozzolanic reactivity of lithium slag was induced after 7 days, and 10–20% LS gained sufficient SAI to be characterised as highly reactive systems at 28 days. In addition, 30% and 60% LS induced pozzolanic reactivity at 90 days, and systems became highly and moderately pozzolanic reactive. In contrast, the SAI of 40–50% LS was in between 65 and 100% at 7, 28, 90 days. Interestingly, the increase in the SAIs of 10–30% LS characterised the mixes from moderately pozzolanic to highly pozzolanic systems at 28 and 90 days, where the probability of gaining strength is likely to be exclusive from RILEM TC 267-TRM phase 3 [99] dataset for 52 different types of SCMs. The 7 days R^3 test total heat provided a high correlation (R^2 = 0.63–0.72) with SAIs, while RILEM TC 267-TRM phase 3 [99] mentioned $R^2 > 0.70$ for wide range of pozzolans. Therefore, R^3 test provided potential contribution in the characterisation of the strength development of 10–60% LS mortars.

Table 4
Comparison of the pozzolans standard requirements with lithium slag and its products.

Parameters	ASTM C618 [66]	BS 8615-1 [75]	AS 3582.4 [125]	Lithium slag
CaO, max %	–	10	–	7.5
MgO, max %	–	4	5	0.6
Total alkali content (Na_2O eq), max %	–	5	–	1.3
$SiO_2 + Al_2O_3 + Fe_2O_3$, min %	70	70	70	77.2
SO_3, max %	4	3	3	5.6
LOI, max %	10	7	6	7.8[a]
Moisture content, max %	3	–	0.5	0.02
Retained on 45 μm sieve, max %	34	40	50	45
Water requirement (% of control), max %	115	115	120	105[b]
7 days SAI, min %	75	–	75	77[b]
28 days SAI, min %	75	75	75	93[b]
90 days SAI, min %	–	85	–	92[b]

[a] LOI at 750 °C as per ASTM C311 [68].
[b] The water requirement and SAIs of 40% LS mortar are presented.

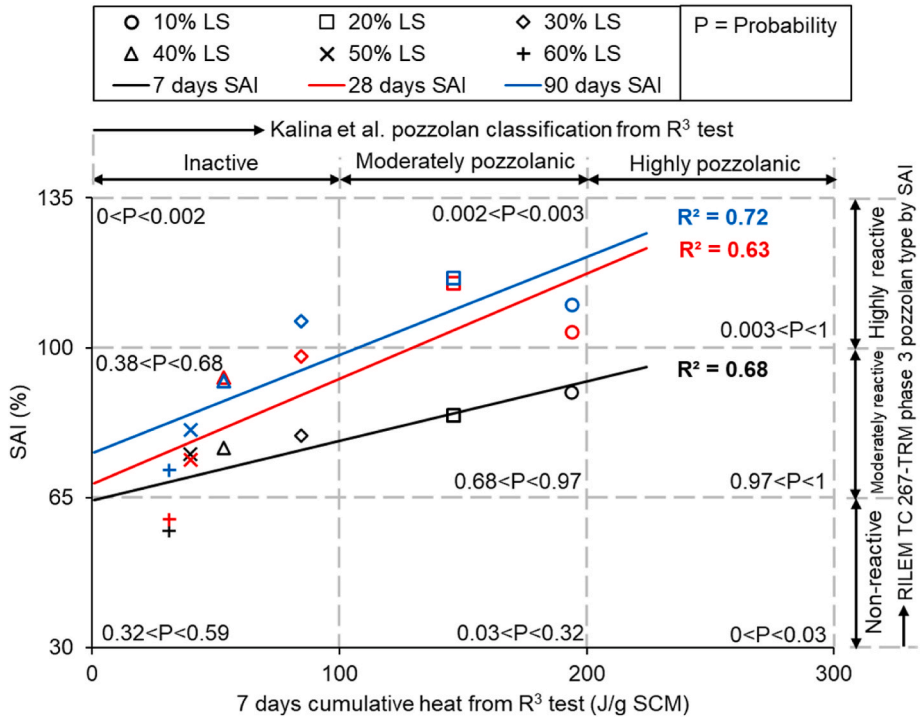

Fig. 14. Assessment of pozzolanicity of 10–60% LS at 7, 28, and 90 days SAIs with 7 days R^3 test cumulative hydration heat.

6. Conclusions

In this study, for the first time, the pozzolanic activity of lithium slag was assessed through different chemical tests and investigations of the development of amorphous, amorphous intermediate, and crystalline hydration products of lime reacted lithium slag at different ages. The following conclusions are extracted from the results and discussions.

- The raw lithium slag possessed 31.6% amorphous phase, and mostly contained Na, Ca, and Mg bearing aluminosilicate phases, which is consistent with other commonly used pozzolans. Therefore, it is considered suitable to use as a pozzolanic material.
- The unsaturated lime consumption test resulted in 889 mg/g pozzolanic activity, and the electrical conductivity test reached reaction equilibrium at 235.5 h. The significance of the results obtained from unsaturated lime consumption and electrical conductivity tests as vital precursors requires conducting Frattini, SAI, and R^3 tests to assess the extent of cement replacement needed to achieve optimum pozzolanic activity in lithium slag.
- In this study, 40% lithium slag as a SCM could react with 79% CaO of cement proportion, provided 93% SAI at 28 days, produced 53.1 J/g SCM hydration heat with portlandite at 7 days. However, using 20% lithium slag as an SCM yielded maximum SAI, while higher percentages (50–60%) led to reduced strength and hydration heat.
- The development of secondary hydration products from the reaction lithium slag with lime at different stages was assessed by XRD and STEM-EDS. The Na^+, Mg^{2+}, Al^{3+}, K^+, and Fe^{3+} ions in the amorphous aluminosilicate phase of lithium slag are incorporated in C–S–H structure to form a combination of crystalline, amorphous intermediate, and amorphous hydration products forming a dense microstructure.
- The physiochemical and compressive strength properties of lithium slag as a pozzolan meet ASTM C618 [66], BS 8615-1 [75], and AS 3582.4 [125] requirements. This study also found lithium slag to be a competent SCM from the correlation ($R^2 > 0.63$) of R^3 and SAI tests in comparison to RILEM TC 267-TRM phase 3 specifications [99].

A direct correlation between various pozzolanic activity tests in the characterisation of lithium slag as a SCM may produce ambiguity due to differences in the working methods, curing conditions, lime pozzolan ratios, water to binder ratios, reaction mechanisms, and alkali release by pozzolan [33,127–129]. Therefore, mechanical and durability properties of concrete are required to assess the effectiveness of lithium slag as a SCM for further understanding.

Declaration of competing interest

The authors declare that they have no known competing financial interests or personal relationships that could have appeared to influence the work reported in this paper.

Data availability

Data will be made available on request.

Acknowledgements

This research was financially supported by the Australian Research Council (ARC) discovery project DP200102784.

Appendix

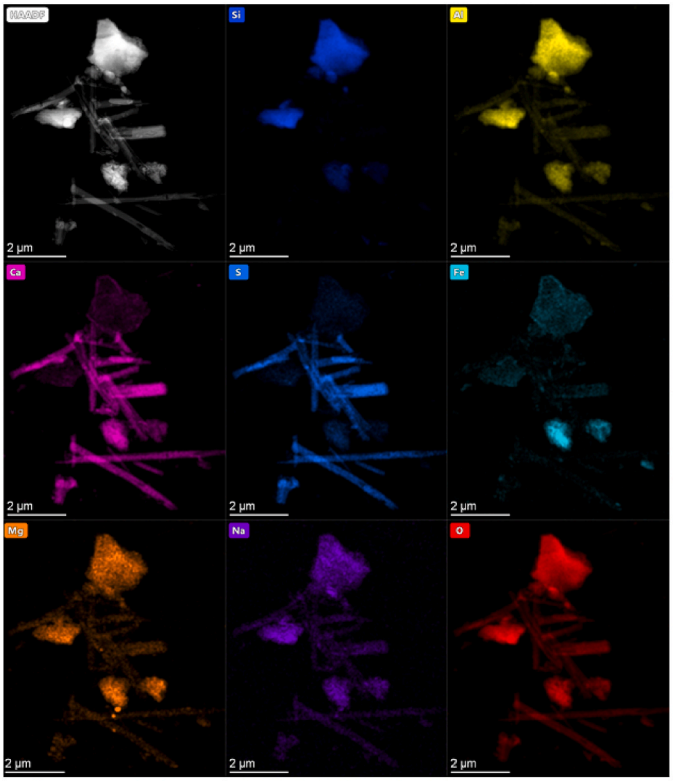

(a)

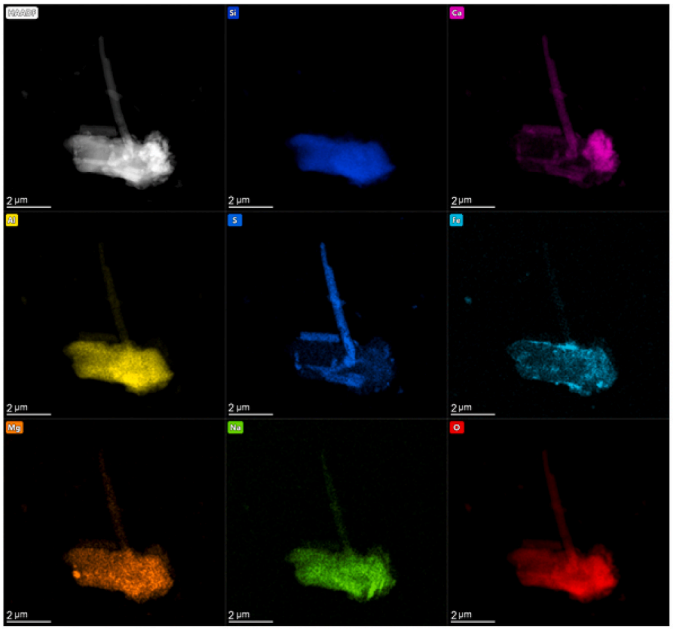

(b)

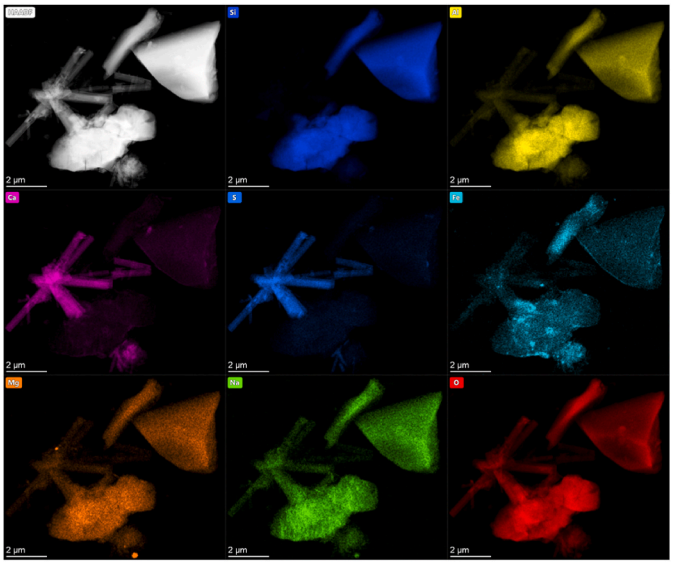

(c)

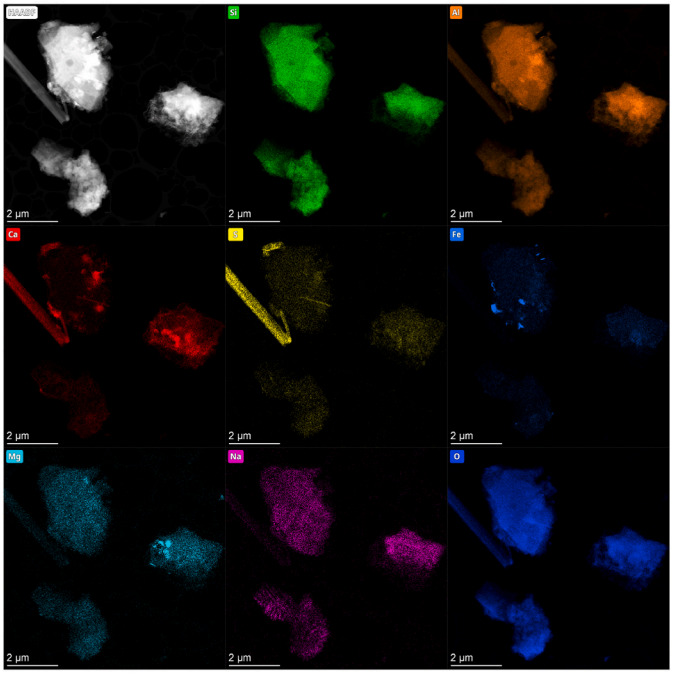

(d)

Fig. A. STEM-EDS colour mapping of the elements of unsaturated lime reacted lithium slag at 1 day (a), 3 days (b), 7 days (c), and (d) 56 days.

References

[1] S.A. Rahman, F.U.A. Shaikh, P.K. Sarker, A comprehensive review of properties of concrete containing lithium refinery residue as partial replacement of cement, Construct. Build. Mater. 328 (2022), 127053.
[2] Z. He, L.-y. Li, S. Du, Mechanical properties, drying shrinkage and creep of concrete containing lithium slag, Construct. Build. Mater. 147 (2017) 296–304.
[3] Z. He, S. Du, D. Chen, Microstructure of ultra high performance concrete containing lithium slag, J. Hazard Mater. 353 (2018) 35–43.
[4] B. Li, et al., Products and properties of steam cured cement mortar containing lithium slag under partial immersion in sulfate solution, Construct. Build. Mater. 220 (2019) 596–606.
[5] M. Haigh, et al., Development of new high performance supplementary cementitious material – a lithium production by-product, in: CIA Binnual Coference, Concrete Institute of Australia (CIA), Australia, 2013.
[6] B. Munn, I. Dumitru, D. Maree, Assessment of the performance of new supplementary cementitious materials from lithium production residues, in: CIA Binnual Coference, Concrete Institute of Australia (CIA), Melbourne, Australia, 2019.
[7] Z. He, et al., Hydration and microstructure of concrete containing high volume lithium slag, Mater. Express 10 (3) (2020) 430–436.
[8] M. Zhai, et al., Hydration properties and kinetic characteristics of blended cement containing lithium slag powder, J. Build. Eng. 39 (2021).
[9] T. Zhang, et al., Effect of TIPA on mechanical properties and hydration properties of cement-lithium slag system, J. Environ. Manag. 276 (2020), 111274.
[10] J. Dong, et al., Function and effect of borax on magnesium phosphate cement prepared by magnesium slag after salt lake lithium extraction, Construct. Build. Mater. 366 (2023), 130280.
[11] X. Gu, et al., Synergistic effect and mechanism of lithium slag on mechanical properties and microstructure of steel slag-cement system, Construct. Build. Mater. 396 (2023), 131768.
[12] Y. Zhang, et al., Improving the performance of ultra-high performance concrete containing lithium slag by incorporating limestone powder, J. Build. Eng. 72 (2023), 106610.
[13] M. Zhou, et al., Insight to workability, compressive strength and microstructure of lithium slag-steel slag based cement under standard condition, J. Build. Eng. (2023), 107076.
[14] S.M.A. Rahman, et al., Fresh state and hydration properties of high-volume lithium slag cement composites, Mater. Struct. 56 (4) (2023) 91.
[15] Q. Luo, et al., Lithium slag-based geopolymer synthesized with hybrid solid activators, Construct. Build. Mater. 365 (2023), 130070.
[16] Y. Tian, et al., Improving the rheological behavior of alkali-activated slag pastes by using low surface free energy mineral admixtures, Construct. Build. Mater. 392 (2023), 131879.
[17] U. Javed, F.U.A. Shaikh, P.K. Sarker, Microstructural investigation of lithium slag geopolymer pastes containing silica fume and fly ash as additive chemical modifiers, Cement Concr. Compos. 134 (2022), 104736.
[18] A. Karrech, et al., Sustainable geopolymer using lithium concentrate residues, Construct. Build. Mater. 228 (2019), 116740.
[19] J. Fan, et al., Heavy metals immobilization of ternary geopolymer based on nickel slag, lithium slag and metakaolin, J. Hazard Mater. 453 (2023), 131380.
[20] Y. He, et al., Lithium slag and fly ash-based binder for cemented fine tailings backfill, J. Environ. Manag. 248 (2019), 109282.
[21] Y. He, et al., Mechanical and environmental characteristics of cemented paste backfill containing lithium slag-blended binder, Construct. Build. Mater. (2021) 271.
[22] S. Dong, et al., Investigation of the performance of cement mortar incorporating lithium slag as a super-fine aggregate, Front. Mater. 10 (2023), 1134622.
[23] C. Li, et al., Preparation of lightweight ceramsite from solid waste lithium slag and fly ash, Construct. Build. Mater. 398 (2023), 132419.
[24] P.H.R. Borges, et al., Lithium aluminosilicate residue as raw material in the production of sustainable concrete masonry units: a Brazilian case, Open Construct. Build Technol. J. 10 (1) (2016) 418–430.
[25] B. Ayati, et al., Acid activated smectite clay as pozzolanic supplementary cementitious material, Cement Concr. Res. 162 (2022), 106969.
[26] P.K. Choubey, et al., Advance review on the exploitation of the prominent energy-storage element: lithium. Part I: from mineral and brine resources, Miner. Eng. 89 (2016) 119–137.
[27] Q. Yan, et al., Extraction of lithium from lepidolite by sulfation roasting and water leaching, Int. J. Miner. Process. 110–111 (2012) 1–5.
[28] L.I. Barbosa, et al., Lithium extraction from β-spodumene through chlorination with chlorine gas, Miner. Eng. 56 (2014) 29–34.
[29] Z. Liu, et al., A green route to sustainable alkali-activated materials by heat and chemical activation of lithium slag, J. Clean. Prod. 225 (2019) 1184–1193.
[30] R. Walker, S. Pavía, Physical properties and reactivity of pozzolans, and their influence on the properties of lime–pozzolan pastes, Mater. Struct. 44 (2011) 1139–1150.
[31] H. Wang, X. Liu, Z. Zhang, Pozzolanic activity evaluation methods of solid waste: a review, J. Clean. Prod. 402 (2023), 136783.
[32] E. Villar-Cociña, et al., Kinetics of the pozzolanic reaction between lime and sugar cane straw ash by electrical conductivity measurement: a kinetic–diffusive model, Cement Concr. Res. 33 (4) (2003) 517–524.
[33] S. Donatello, M. Tyrer, C. Cheeseman, Comparison of test methods to assess pozzolanic activity, Cement Concr. Compos. 32 (2) (2010) 121–127.
[34] M.P. Luxán, F. Madruga, J. Saavedra, Rapid evaluation of pozzolanic activity of natural products by conductivity measurement, Cement Concr. Res. 19 (1) (1989) 63–68.
[35] S. Sinthaworn, P. Nimityongskul, Effects of temperature and alkaline solution on electrical conductivity measurements of pozzolanic activity, Cement Concr. Compos. 33 (5) (2011) 622–627.
[36] J. Payá, et al., Enhanced conductivity measurement techniques for evaluation of fly ash pozzolanic activity, Cement Concr. Res. 31 (1) (2001) 41–49.
[37] P. Hewlett, M. Liska, Lea's Chemistry of Cement and Concrete, Butterworth-Heinemann, 2019.
[38] K. Celik, et al., High-volume natural volcanic pozzolan and limestone powder as partial replacements for portland cement in self-compacting and sustainable concrete, Cement Concr. Compos. 45 (2014) 136–147.
[39] He, Y., et al., Characteristic and Mechanism of the Pozzolanic Activity of Melted-Quenched Lithium Slag Modified with Na2sio3. Available at: SSRN 4131236.
[40] J. Li, S. Huang, Recycling of lithium slag as a green admixture for white reactive powder concrete, J. Mater. Cycles Waste Manag. 22 (6) (2020) 1818–1827.
[41] Y. He, et al., Mechanism and assessment of the pozzolanic activity of melting-quenching lithium slag modified with MgO, Construct. Build. Mater. 363 (2023), 129692.
[42] Y. Zhang, et al., Improving the performance of ultra-high performance concrete containing lithium slag by incorporating limestone powder, J. Build. Eng. (2023), 106610.
[43] S. Li, et al., Effect of mineral-generated lithium slag on the properties of magnesium oxychloride cement, Crystals 13 (3) (2023) 513.
[44] Y. He, et al., Effects of TEA on rheological property and hydration performance of lithium slag-cement composite binder, Construct. Build. Mater. 318 (2022), 125757.
[45] As 3972, General Purpose and Blended Cements, 2010. Standards Australia: Australia.
[46] J. Bodycomb, in: M. Panalytical (Ed.), Webinar: PST & BDAS - an Acronym Approach to Laser Diffraction Method Development, 2019. https://www.malvernpanalytical.com/es/learn/events-and-training/webinars/w190815pst (registration/login required).
[47] ASTM C778, Standard Specification for Standard Sand, American Society for Testing and Materials, USA, 2021.
[48] 1, AS 1141, Methods for Sampling and Testing Aggregates, 2015. Standards Australia: Australia.
[49] L.J. Poppe, et al., A laboratory manual for X-ray powder diffraction, US Geolo. Surv. open-file Rep. 1 (41) (2001) 1–88.
[50] R. Snellings, A. Bazzoni, K. Scrivener, The existence of amorphous phase in Portland cements: physical factors affecting Rietveld quantitative phase analysis, Cement Concr. Res. 59 (2014) 139–146.
[51] B.H. Toby, R factors in Rietveld analysis: how good is good enough? Powder Diffr. 21 (1) (2006) 67–70.
[52] M.G. Aylmore, et al., Assessment of a spodumene ore by advanced analytical and mass spectrometry techniques to determine its amenability to processing for the extraction of lithium, Miner. Eng. 119 (2018) 137–148.
[53] M. Fleet, et al., Rock-forming Minerals: Micas, Geological Society of London, 1978.
[54] J.J. Norton, Iron in spodumene of different mineral assemblages in Black Hills pegmatites, South Dakota, Econ. Geol. 77 (3) (1982) 702–708.
[55] G.E. Christidis, Advances in the Characterization of Industrial Minerals, 9, The Mineralogical Society of Great Britain and Ireland, 2011.
[56] ASTM 1872, Standard Test Method For Thermogravimetric Analysis of Hydraulic Cement, American Society for Testing Materials, United States, 2018.
[57] L. Alarcon-Ruiz, et al., The use of thermal analysis in assessing the effect of temperature on a cement paste, Cement Concr. Res. 35 (3) (2005) 609–613.
[58] G. Platret, Suivi de l'hydratation du ciment et de l'évolution des phases solides dans les bétons par analyse thermique, caractéristiques microstructurales et propriétés relativesa la durabilité des bétons. méthodes de mesure et d'essai de laboratoire, 58, Méthode d'essai, 2002.
[59] D. Jo, et al., Gypsum content determination in Portland cements by thermogravimetry, J. Therm. Anal. Calorim. 123 (2) (2016) 1053–1062.
[60] S.A. Bernal, et al., Characterization of supplementary cementitious materials by thermal analysis, Mater. Struct. 50 (1) (2016) 26.
[61] S. Seraj, Evaluating Natural Pozzolans for Use as Alternative Supplementary Cementitious Materials in Concrete, 2014.
[62] En 27888, Water quality, in: Determination of Electrical Conductivity, CEN - European Committee for Standardization, UK, 1993, pp. 1–8.
[63] E. Villar-Cocina, et al., Kinetics of the water absorption in GGBS-concretes: a capillary-diffusive model, Comput. Concr. Int. J. 2 (1) (2005) 19–30.
[64] BS EN 196-5, Methods of Testing Cement Part 5: Pozzolanicity Test for Pozzolanic Cement, British Standard, UK, 2011.
[65] ASTM C109/C109M, *S*tandard Test Method for Compressive Strength of Hydraulic Cement Mortars (Using 2-in. Or [50 Mm] Cube Specimens), American Society for Testing Materials, USA, 2020.
[66] ASTM C618, Standard Specification for Coal Fly Ash and Raw or Calcined Natural Pozzolan for Use in Concrete, American Society for Testing Materials, USA, 2019.
[67] ASTM 1437, Standard Test Method for Flow of Hydraulic Cement Mortar, American Society for Testing Materials, USA, 2020.
[68] ASTM C311/C311M, Standard Test Methods for Sampling and Testing Fly Ash or Natural Pozzolans for Use in Portland-Cement Concrete, American Society for Testing Materials, USA, 2018.
[69] ASTM 1897, Standard Test Methods for Measuring The Reactivity of Supplementary Cementitious Materials by Isothermal Calorimetry and Bound

Water Measurements, American Society for Testing Materials, United States of America, 2020.
[70] F. Avet, et al., Report of RILEM TC 267-TRM phase 2: optimization and testing of the robustness of the R3 reactivity tests for supplementary cementitious materials, Mater. Struct. 55 (3) (2022) 92.
[71] S. Al-Shmaisani, et al., Critical assessment of rapid methods to qualify supplementary cementitious materials for use in concrete, Cement Concr. Res. 153 (2022), 106709.
[72] J. Zhang, G.W. Scherer, Comparison of methods for arresting hydration of cement, Cement Concr. Res. 41 (10) (2011) 1024–1036.
[73] K. Scrivener, R. Snellings, B. Lothenbach, A Practical Guide to Microstructural Analysis of Cementitious Materials, 540, Crc Press, Boca Raton, FL, USA, 2016.
[74] M. Chabannes, et al., Performance and microstructure development of lime–calcined fluvial sediment binders under different curing conditions, Cement Concr. Res. 160 (2022), 106903.
[75] BS 8615-1, Specification for Pozzolanic Materials for Use with Portland Cement Natural Pozzolana and Natural Calcined Pozzolana, British standard, 2019.
[76] F. Pacheco-Torgal, et al., Biopolymers and Biotech Admixtures for Eco-Efficient Construction Materials, Woodhead Publishing, 2016.
[77] J. Skibsted, R. Snellings, Reactivity of supplementary cementitious materials (SCMs) in cement blends, Cement Concr. Res. 124 (2019), 105799.
[78] D. Li, et al., Study on the pozzolanic activity of ultrafine circulating fluidized-bed fly ash prepared by jet mill, Fuel 291 (2021), 120220.
[79] S. Nie, R.M. Thomsen, J. Skibsted, Impact of Mg substitution on the structure and pozzolanic reactivity of calcium aluminosilicate (CaO-Al2O3-SiO2) glasses, Cement Concr. Res. 138 (2020), 106231.
[80] G. Laforest, J. Duchesne, Immobilization of chromium (VI) evaluated by binding isotherms for ground granulated blast furnace slag and ordinary Portland cement, Cement Concr. Res. 35 (12) (2005) 2322–2332.
[81] M. Bagheri, et al., Effect of different ions on dissolution rates of silica and feldspars at high pH, Cement Concr. Res. 152 (2022), 106644.
[82] T. Hertel, J. Neubauer, F. Goetz-Neunhoeffer, Study of hydration potential and kinetics of the ferrite phase in iron-rich CAC, Cement Concr. Res. 83 (2016) 79–85.
[83] T.M.S. Agra, et al., Characterizing and processing a kaolinite-rich water treatment sludge for use as high-reactivity pozzolan in cement manufacturing, Appl. Clay Sci. 236 (2023), 106870.
[84] R. Walker, S. Pavía, Physical properties and reactivity of pozzolans, and their influence on the properties of lime–pozzolan pastes, Mater. Struct. 44 (6) (2011) 1139–1150.
[85] J. Li, et al., A new method to rapidly evaluate the activity of volcanic ash materials, Cement Concr. Compos. 135 (2023), 104833.
[86] X. Li, et al., Reactivity tests for supplementary cementitious materials: RILEM TC 267-TRM phase 1, Mater. Struct. 51 (6) (2018) 151.
[87] S. Donatello, et al., Effect of milling and acid washing on the pozzolanic activity of incinerator sewage sludge ash, Cement Concr. Compos. 32 (1) (2010) 54–61.
[88] A. Tironi, et al., Assessment of pozzolanic activity of different calcined clays, Cement Concr. Compos. 37 (2013) 319–327.
[89] A. Tironi, et al., Kaolinitic calcined clays: factors affecting its performance as pozzolans, Construct. Build. Mater. 28 (1) (2012) 276–281.
[90] M. Moesgaard, et al., Calcium aluminosilicate glasses as supplementary cementitious materials, Glass Technol. Eur. J. Glass Sci. Technol. 51 (5) (2010) 183–190.
[91] A. Dauzeres, et al., Magnesium perturbation in low-pH concretes placed in clayey environment—solid characterizations and modeling, Cement Concr. Res. 79 (2016) 137–150.
[92] Y. Jia, et al., Effect of CaO on the reaction process of MgO-SiO2-H2O cement pastes, Mater. Lett. 192 (2017) 48–51.
[93] M. Bedeaux, et al., Atomic structure and phase assemblages in novel M-(N)-A-S-H materials, Cement Concr. Res. 142 (2021), 106336.
[94] R. Xiao, et al., Analytical investigation of phase assemblages of alkali-activated materials in CaO-SiO2-Al2O3 systems: the management of reaction products and designing of precursors, Mater. Des. 194 (2020), 108975.
[95] K. Pimraksa, et al., Cement mortars hybridized with zeolite and zeolite-like materials made of lignite bottom ash for heavy metal encapsulation, J. Clean. Prod. 41 (2013) 31–41.
[96] B. Liu, et al., Understanding the early reaction and structural evolution of alkali activated slag optimized using K-A-S-H nanoparticles with varying K2O/SiO2 ratios, Compos. B Eng. 200 (2020), 108311.
[97] K. De Weerdt, et al., Phase changes in cementitious materials exposed to saline solutions, Cement Concr. Res. 165 (2023), 107071.
[98] BS EN 450-1, Fly ash for concrete, in: Part 1: Definition, Specifications and Conformity Criteria provided by S&P Global Licensee=/, User=, No Reproduction or Networking Permitted without License from S&P Global Not for Resale, British standard, Belgium, 2012.
[99] D. Londono-Zuluaga, et al., Report of RILEM TC 267-TRM phase 3: validation of the R3 reactivity test across a wide range of materials, Mater. Struct. 55 (5) (2022) 142.
[100] R. Snellings, et al., Rapid, robust, and relevant (R3) reactivity test for supplementary cementitious materials, ACI Mater. J. 116 (4) (2019).
[101] A.H. Mahmood, et al., The efficiency of recycled glass powder in mitigating the alkali-silica reaction induced by recycled glass aggregate in cementitious mortars, Mater. Struct. 55 (6) (2022) 156.
[102] A. Hamdan, et al., The changes in the reaction kinetics and phase assemblage of sodium silicate-activated CaO-MgO-Al2O3-SiO2 glasses induced by the Al replacement by Mg, Cement Concr. Res. 166 (2023), 107103.
[103] A. Hamdan, et al., The intrinsic role of network modifiers (Ca versus Mg) in the reaction kinetics and microstructure of sodium silicate-activated CaO-MgO-Al2O3-SiO2 glasses, Cement Concr. Res. 164 (2023), 107058.
[104] P.P. Sivakumar, et al., Reactivity assessment of modified ferro silicate slag by R3 method, Appl. Sci. 11 (1) (2021) 366.
[105] C. Hesse, F. Goetz-Neunhoeffer, J. Neubauer, A new approach in quantitative in-situ XRD of cement pastes: correlation of heat flow curves with early hydration reactions, Cement Concr. Res. 41 (1) (2011) 123–128.
[106] R.D. Kalina, et al., False positives in ASTM C618 specifications for natural pozzolans, ACI Mater. J. 116 (1) (2019) 165–172.
[107] M. García-Maté, et al., Effect of calcium sulfate source on the hydration of calcium sulfoaluminate eco-cement, Cement Concr. Compos. 55 (2015) 53–61.
[108] L.G. Baquerizo, et al., Hydration states of AFm cement phases, Cement Concr. Res. 73 (2015) 143–157.
[109] Y. Jeong, et al., The effect of elevated curing temperatures on high ye'elimite calcium sulfoaluminate cement mortars, Materials 12 (7) (2019) 1072.
[110] V. Bonavetti, V. Rahhal, E. Irassar, Studies on the carboaluminate formation in limestone filler-blended cements, Cement Concr. Res. 31 (6) (2001) 853–859.
[111] Q. Zheng, et al., In situ TEM observation of calcium silicate hydrate nanostructure at high temperatures, Cement Concr. Res. 149 (2021), 106579.
[112] S. Irico, et al., A solid-state NMR and X-ray powder diffraction investigation of the binding mechanism for self-healing cementitious materials design: the assessment of the reactivity of sodium silicate based systems, Cement Concr. Compos. 76 (2017) 57–63.
[113] S.J. Barnett, et al., XRD, EDX and IR analysis of solid solutions between thaumasite and ettringite, Cement Concr. Res. 32 (5) (2002) 719–730.
[114] K. Tosun, B. Baradan, Effect of ettringite morphology on DEF-related expansion, Cement Concr. Compos. 32 (4) (2010) 271–280.
[115] G. Zhang, et al., Adding hydrated lime for improving microstructure and mechanical properties of mortar for ultra-high performance concrete, Cement Concr. Res. 167 (2023), 107130.
[116] A. Grudemo, The micrcostructure of hardened cement paste, in: Chemistry of Cemnet, National Bureau of Standards, Washington, USA, October .
[117] Y. Wang, et al., Intrinsic sulfuric acid resistance of C-(N)-A-S-H and N-A-S-H gels produced by alkali-activation of synthetic calcium aluminosilicate precursors, Cement Concr. Res. 165 (2023), 107068.
[118] H. Tian, et al., Influence of foreign ions on calcium silicate hydrate under hydrothermal conditions: a review, Construct. Build. Mater. 301 (2021), 124071.
[119] W. NocuÒ-Wczelik, Effect of Na and Al on the phase composition and morphology of autoclaved calcium silicate hydrates☆☆This paper was originally submitted to Advanced Cement Based Materials. The paper was received at the Editorial Office of Cement and Concrete Research on 5 November 1998 and accepted in final form on 16 July 1999, Cement Concr. Res. 29 (11) (1999) 1759–1767.
[120] G. Fang, M. Zhang, Multiscale micromechanical analysis of alkali-activated fly ash-slag paste, Cement Concr. Res. 135 (2020), 106141.
[121] I. Jawed, S. Goto, R. Kondo, Hydration of tetracalcium aluminoferrite in presence of lime and sulfates, Cement Concr. Res. 6 (4) (1976) 441–453.
[122] W.-G. Lee, M.-S. Song, CO2 adsorption reactions of synthetic calcium aluminum ferrite (CAF), Appl. Sci. 12 (13) (2022) 6677.
[123] S. Duan, et al., Investigation into the synergistic effects in hydrated gelling systems containing fly ash, desulfurization gypsum and steel slag, Construct. Build. Mater. 187 (2018) 1113–1120.
[124] A. Baldermann, et al., Uptake of aqueous heavy metal ions (Co2+, Cu2+ and Zn2+) by calcium-aluminium-silicate-hydrate gels, Cement Concr. Res. 147 (2021), 106521.
[125] AS 3582.4, Supplementary Cementitious Materials, Part 4: Pozzolans — Manufactured (FOREIGN STANDARD), 2022. Standards Australia: Australia.
[126] Z.-h. He, L.-y. Li, S.-g. Du, Mechanical properties, drying shrinkage, and creep of concrete containing lithium slag, Construct. Build. Mater. 147 (2017) 296–304.
[127] R. Snellings, K.L. Scrivener, Rapid screening tests for supplementary cementitious materials: past and future, Mater. Struct. 49 (8) (2016) 3265–3279.
[128] R.T. Thorstensen, P. Fidjestol, Inconsistencies in the pozzolanic strength activity index (SAI) for silica fume according to EN and ASTM, Mater. Struct. 48 (12) (2015) 3979–3990.
[129] X. Li, et al., Reactivity tests for supplementary cementitious materials: RILEM TC 267-TRM phase 1, Mater. Struct. 51 (2018) 1–14.